Design of a Hydraulic Bulge Test Apparatus

by

Cheok Wei Koh

B.S., Naval Architecture and Ocean Engineering
University of Tokyo, 2000

Submitted to the Department of Mechanical Engineering
in Partial Fulfillment of the Requirements for the Degree of

Master of Science in Naval Architecture and Marine Engineering

at the

Massachusetts Institute of Technology

Feb 2008
[February 2008]

Signature of Author .....
Department of Mechanical Engineering
January 18, 2008

Certified by .....
.....
Tomasz Wierzbicki
Professor of Applied Mechanics
Director, Impact and Crashworthiness Laboratory

Accepted by .....
.....
Lallit Anand
Chairman, Department Committee on Graduate Students

Design of a Hydraulic Bulge Test Apparatus

by

Cheok Wei Koh

B.S., Naval Architecture and Ocean Engineering
University of Tokyo, 2000

Submitted to the Department of Mechanical Engineering on January 18, 2008,
in Partial Fulfillment of the Requirements for the
Degree of Master of Science in Naval Architecture and Marine Engineering

ABSTRACT

The various equi-biaxial tension tests for sheet metal were studied and compared to determine the most appropriate equipping in the Impact and Crashworthiness Laboratory, MIT, for the testing of Advanced High Strength Steel. The hydraulic bulge test was identified as the most economical solution. The equipment was designed to accommodate material strength of up to 1000MPa with plate thickness between 1.0mm and 1.8mm. The design process is explained in detail with focus on the challenges faced.

The closed-form solution for the hydraulic bulge test was also derived. Two methods of deriving the stress-strain relationship in the material were also proposed. The first method uses the optical measuring system to determine displacement and surface strain distribution. The second method uses geometrical approximations and dome height measurements.

A new experimental technique and step-by-step procedure were also developed. Tests were successfully conducted using galvanized steel to demonstrate the effectiveness of the hydraulic bulge test apparatus in achieving the equi-biaxial stress state in sheet metal.

Thesis Supervisor: Tomasz Wierzbicki
Title: Professor of Applied Mechanics

Acknowledgement

First and foremost, I would like to thank Professor Tomasz Wierzbicki for accepting my request to be my master thesis advisor for the past one year. I deeply appreciate his advice, guidance and patience in the many discussions we had. I am also thankful to have Assistant Professor Dirk Mohr from Ecole Polytechnique, France, review my design and give valuable advice.

I would also like to thank The Hope Group for providing all the materials and expertise in the construction of the apparatus, with special thanks to the engineers - Eric Brockway and Paul Daniels for their constant support. I would like to extend my thanks to Steve Forti and his team of machinists from Mass Bay Engineering Co. for a fine job in the fabrication of the test chamber.

Within the MIT community, I would like to thank Sheila McNary for her efficient administrative support, and Stephen Rudolph for his technical advice. I have also learnt a lot through the interaction with my colleagues, namely Mr Jongmin Shim, Ms Allison Beese and Mr Meng Luo from the Impact and Crashworthiness Laboratory (ICL). Special thanks to Dr Yuanli Bai and Mr Carey Walters who have helped in my understanding of the subject matter through their sharing of experiences in the various experimental techniques. I also treasure the advice and friendship of Dr Keun-Hwan Kim, from POSCO (a member of the Advance High Strength Steel (AHSS) Consortium initiated by ICL) in the exchange of views and experiences.

Lastly, I want to express my deepest gratitude and appreciation to my beloved wife, Kiat Yeng, for the sacrifices she made to accompany me throughout my 17 months in MIT. This thesis could not have been done without her love and constant support.

Contents

List of Figures

List of Tables

Chapter 1

Introduction

1.1 Motivation

Sheet metal is one of the most commonly found semi-finished products used in shipbuilding, aerospace, automobile industries and domestic applications. It forms the basic structural support for these applications and the material properties are essential for safe and efficient design of the product. For example, in shipbuilding, many classification societies have rules which dictate the material properties and usage for safe operations. In today's competitive world, these experience-based criteria needs to be challenged and boundaries need to be pushed to achieve higher cost effectiveness. This is particularly significant in the transportation industries as lighter weight means lower fuel consumption and a host of other advantages, such as higher speed, more cargo space, etc. Furthermore, in the production process, the structures usually involve combinations of complex shapes, which are achieved with sheet metal forming. The forming process takes advantage of the material ductility by plastically deforming the sheet metal into the required shape. However, with increasing plastic deformation, there is the risk of necking followed by ductile fracture, which is a common failure mechanism in sheet metal structures. In certain less ductile materials, fracture may occur before necking. Nonetheless, with a good knowledge of the design and forming process as well as the material properties, catastrophic structural failures can be predicted and avoided. As full-scale tests are costly and time-consuming, it is common practice to perform intrinsic tests to determine the Forming Limit Diagram (FLD) of the material and make use of simulation software to perform detailed production design.

The development of the FLD requires a variety of tests to determine the yield locus

for the sheet metal. The current industrial techniques used include the hydraulic bulge test, biaxial compression tests on adhesively bonded sheet laminate specimens, cruciform specimen biaxial tension and thin tubes subjected to hydrostatic pressure and tension. From these tests, the entire yield locus comprising uni-axial compression, pure shear, uni-axial tension, plane strain, stretch forming and equi-biaxial tension can be derived. The Impact and Crashworthiness Laboratory (ICL) at MIT has developed a new experimental method for the testing of thin specimens under transverse plane strain conditions (Mohr and Oswald, 2007) which is able to construct almost the entire yield locus except the region of equi-biaxial tension or compression. Therefore, it would be appropriate to adopt the hydraulic bulge test to accurately determine this missing range, as it has a simple design and the effect of friction is absent as compared to the Nakazima Punch Test.

There are many materials being developed to meet specific requirements. More recent examples are the Advanced High Strength Steels (AHSS) designed for automobile applications. With these new materials of extremely high tensile strength, existing testing apparatus would have to be re-evaluated and modified to accommodate them. This is a good opportunity to design a new testing apparatus to be able to perform tests to such extremes.

1.2 Objective

The objective of this thesis is to develop a hydraulic bulge test apparatus for determining the yield locus in the region of equi-biaxial tension for most thin sheet metal, including the AHSS. This information can then be used in the calibration of the new plasticity model for the material proposed by Bai and Wierzbicki (2007).

1.3 Overview

This thesis comprises five chapters discussing topics from fracture criteria and experimental techniques for sheet necking and fracture to the design of experiment and results analysis for related sheets. The appendices contain the detailed design of the apparatus, experimental procedures and formulae derivations.

Chapter 1 provides an introduction to the motivation and objective of this thesis, and a broad overview of its content.

Chapter 2 reviews the various plasticity models used in engineering applications and focuses on the new plasticity model proposed by Bai and Wierzbicki (2007). This model defines the fracture locus as a monotonic function of the stress triaxiality parameter η, and an asymmetric function of the lode angle parameter ξ. Various experimental techniques used in sheet necking and fracture, including the strengths and limitations of each technique are also discussed.

Chapter 3 steps through the design and experimental process of this hydraulic bulge test apparatus from the analysis of needs to the design parameters, followed by experimental procedures and data processing. The detailed design of the apparatus is in Appendix A.

Chapter 4 provides the theoretical analysis of the design based on sheet metal. Numerical analysis is also performed using the commercial code, Abaqus, to determine the force-displacement and stress-strain relationship. The results of a demonstrative case, using galvanised steel, are discussed in detail. The experiment procedure is in Appendix B, and the formulae derivation in Appendix C.

Chapter 5 concludes with a summary of the thesis and recommendations for future work on the calibration of the new plasticity model and completing the FFLD.

Chapter 2

Background

2.1 Fracture Criteria for Metal Sheet

There have been many plasticity and fracture models developed till date. Some of the more common fracture criteria used in libraries of material models of non-linear finite element codes are listed below:

a. Constant Equivalent Strains

b. Fracture Forming Limit Diagram (FFLD)

c. Maximum Shear (MS) Stress

d. Johnson-Cook (J-C) Fracture Model

e. Xue-Wierzbicki (X-W) Model

f. Wilkins Model

g. CrachFEM

The detailed evaluation and comparison study of the seven models are explained in Wierzbicki et al (2005). The results are as shown in Figure 1.

From the list of fracture criteria in Section 2.1 and the corresponding results in Figure 1, it is observed that X-W, Wilkins and CrachFEM models have shown good overall predictions and adopted similar concepts of taking into consideration the effect of stress triaxiality and

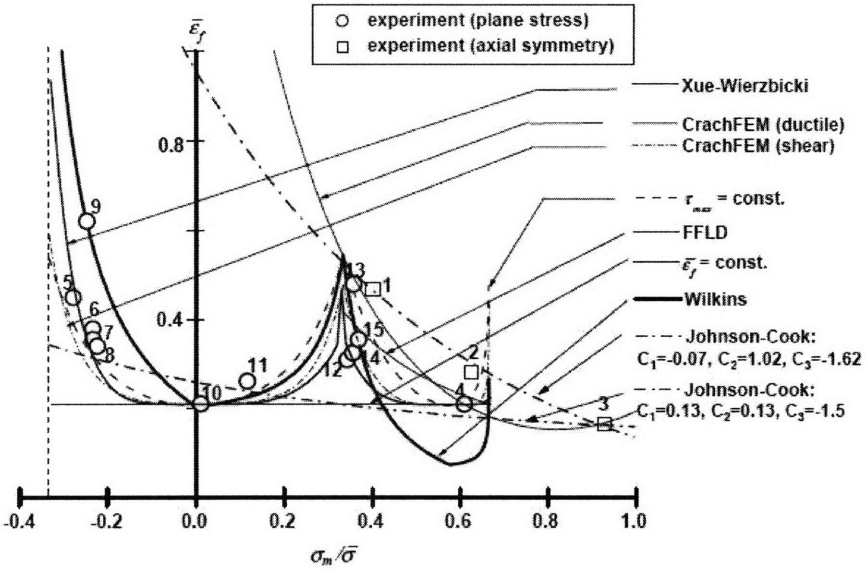

Figure 1: Comparison of the seven fracture criteria with experimental data

deviatoric state defined by the Lode angle θ. There is also growing experimental evidence of this observation by Spitzig and Richmond (1984), Wilson (2002), Barsoum and Faleskog (2006) and tests conducted at the ICL, which led to the proposal of a generalized plasticity model by Bai and Wierzbicki (B-W) (2007):

$$\sigma_{yield} = \bar{\sigma}(\bar{\varepsilon}_p) f_p(\eta) f_\theta(\xi) \tag{1}$$

where

$$\bar{\sigma} = \sqrt{\frac{1}{2}[(\sigma_1 - \sigma_2)^2 + (\sigma_2 - \sigma_3)^2 + (\sigma_3 - \sigma_1)^2]} \quad : \quad \text{equivalent stress}$$

$$\sigma_1, \sigma_2, \sigma_3 \quad : \quad \text{principal stresses}$$

$$\bar{\varepsilon}_p \quad : \quad \text{equivalent plastic strain}$$

$$\eta = \frac{\sigma_m}{\bar{\sigma}} \quad : \quad \text{stress triaxiality}$$

$$\sigma_m = \frac{1}{3}(\sigma_1 + \sigma_2 + \sigma_3) \quad : \quad \text{hydrostatic stress (mean stress)}$$

$$\xi = \frac{27}{2}\frac{J_3}{\bar{\sigma}^3} = \cos 3\theta \quad : \quad \text{lode angle parameter}$$

$$J_3 = s_1 s_2 s_3 \quad : \quad \text{third invariant of deviatoric stress tensor}$$

$$s_1, s_2, s_3 \quad : \quad \text{principal deviatoric stresses}$$

$$f_p(\eta) = 1 - c_\eta(\eta - \eta_0) \tag{2}$$

where c_η is the material constant and η_0 is the reference value of stress triaxiality based on reference test.

The effect of Lode angle parameter was clearly demonstrated in the tensile response of the flat grooved specimen and it was shown by B-W (2007) that function $f_\theta(\xi)$ can be represented by three parameters which defines the plane stress yield locus in the space of principal stresses.

$$f_\theta(\xi) = c_\theta^s + (c_\theta^{ax} - c_\theta^s)(\gamma - \frac{\gamma^{m+1}}{m+1}) \tag{3}$$

where

$$\begin{aligned}
\gamma &= \frac{\cos(\frac{\pi}{6})}{1 - \cos(\frac{\pi}{6})}\left[\frac{1}{\cos(\theta - \frac{\pi}{6})} - 1\right] \\
&= 6.4641(\sec(\theta - \frac{\pi}{6}) - 1) \\
c_\theta^{ax} &= \begin{cases} c_\theta^t & \text{for} \quad \bar{\theta} \geq 0 \\ c_\theta^c & \text{for} \quad \bar{\theta} < 0 \end{cases} \\
c_\theta^s, c_\theta^t, c_\theta^c, m &: \text{material constants}
\end{aligned}$$

The parameters c_θ^s and c_θ^c provide the general shape of the ellipse while m defines the local curvature around the point of equi-biaxial tension. Therefore, with a variety of experiments to cover the entire range of the yield locus, the function $f_\theta(\xi)$ can be calibrated for each material type. The existing capabilities of the ICL could construct almost the entire yield locus except in the region of equi-biaxial tension or compression. It is therefore essential to develop an experimental technique to determine this missing range.

2.2 Experimental Techniques for Sheet Necking and Fracture

In sheet metal forming, there are generally two main categories of tests, namely simulating test method and intrinsic method. Some of the common simulating tests are the Erichsen (1914) and Olsen (1920) punch-stretching methods, Hecker (1974) test, Sachs (1930) wedge

drawing test, Blume (1922), Swift and Chung (1951) deep-drawing methods, Swift (1954) cup-drawing test, Fukui (1939) conical cup test, bending test in ASTM E 290-97a, and Demeri (1981) stretch-bend test. These tests require unique equipment and thus apply only to specific forming processes. On the other hand, the intrinsic method uses material parameters to define a measurement of formability. This results in a generalized formability of a specific material which could be used in many applications. The Forming Limit Diagram (FLD) and its corresponding tests would be discussed in greater detail in the next section.

The Forming Limit Diagram (FLD) and Fracture Forming Limit Diagram (FFLD) determine the limit strains for necking and fracture respectively. As shown in Figure 2, the strain domain covers the pure shear, uni-axial tension, plane strain, stretch forming and equi-biaxial tension, which occurs in industrial sheet metal forming process. These limiting values are achieved through a range of experiments.

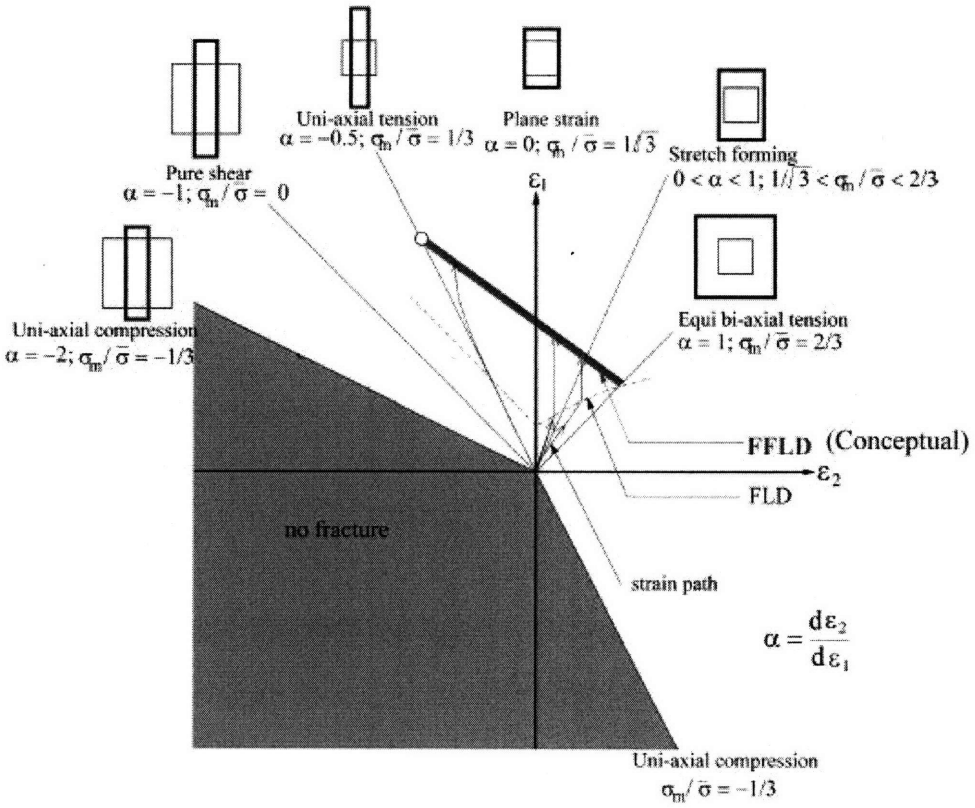

Figure 2: Forming Limit Diagram and Fracture Forming Limit Diagram

Table 1 shows a list of the common tests used. Each test has its own advantages and disadvantages in terms of the complexity of equipment design, specimen design, test range and accuracy, which determines the final cost of developing the FLD and FFLD.

Table 1: Comparison of Different Tests

Type of Test	By (Year)	Equipment	Specimen	Test Range
Uni-axial Tensile Test	Brozzo et al (1972)	General purpose testing machine. **(Adv: simple equipment)**	Rectangular specimen with and without notches of different dimensions and sizes. **(Adv: relatively simple design, relatively easy to manufacture)**	$\varepsilon_2 < 0$ **(Disadv: limited to negative section of FLD)**
Hydraulic Bulge Test	Olsen (1920)	Special hydraulic chamber with hydraulic system and controls. **(Disadv: special equipment)** Circular/elliptical dies. **(Adv: reusability of dies for testing various materials, no friction effect)**	One size circular specimen. **(Adv: simple design, easy to manufacture)**	$\varepsilon_2 > 0$ **(Disadv: limited to positive section of FLD)**
Keeler Punch Stretching Test	Keeler (1961)	General purpose testing machine. **(Adv: simple equipment)** Spherical punches with different radii. **(Adv: reusability of punches for testing various materials. Disadv: complex design and difficult to manufacture)** Use of lubricant **(Disadv: difficulty in determining the degree and effect of friction)**	Rectangular specimen with different width. **(Adv: simple design, easy to manufacture Disadv: wrinkling of specimen)**	$\varepsilon_2 > 0$ **(Disadv: limited to positive section of FLD)**

continued on next page

Table 1 – continued from previous page

Type of Test	By (Year)	Equipment	Specimen	Test Range
Marciniak Test	Marciniak (1971)	General purpose testing machine. **(Adv: simple equipment)** Hollow punches and dies with different cross sections. **(Adv: eliminate measurement errors caused by curvature, reusability of punches for testing various materials Disadv: many complex shapes and difficult to manufacture)**	Circular or rectangular specimen of various sizes. **(Adv: relatively simple design, easy to manufacture)**	$\varepsilon_2 > 0$ **(Disadv: limited to positive section of FLD)**
Nakazima Test	Nakazima et al (1971)	General purpose testing machine. **(Adv: simple equipment)** Hemispherical punch and circular die. **(Adv: reusability of punches for testing various materials)** Use of lubricant **(Disadv: difficulty in determining the degree and effect of friction)**	Rectangular specimen with different width. **(Adv: simple design, easy to manufacture Disadv: wrinkling of specimen)**	Positive and negative range of ε_2 values **(Adv: wide range of values in FLD domain)**
Hasek Test	Hasek (1973)	General purpose testing machine. **(Adv: simple equipment)** Hemispherical punch and circular die. **(Adv: reusability of punches for testing various materials)** Use of lubricant **(Disadv: difficulty in determining the degree and effect of friction)**	Circular specimen with recesses of different radii **(Adv: eliminate wrinkling of specimen, relatively easy to manufacture)**	Positive and negative range of ε_2 values **(Adv: wide range of values in FLD domain)**

continued on next page

Table 1 – continued from previous page

Type of Test	By (Year)	Equipment	Specimen	Test Range
Bi-axial Tensile Test using Cruciform Specimen	Shiratori and Ikegami (1968) Ferron and Makinde (1988) Demmerle and Boehler (1993) Mller and Phlandt (1996) Kuwabara (1998) Hoferlin et al (2000)	Special biaxial testing machine with control system. **(Disadv: complex design, high setup cost)**	Cruciform specimen with thinned gauge section and arms with slits. **(Disadv: complex design, difficult to manufacture)**	Positive and negative range of ε_2 values **(Adv: wide range of values in FLD domain)**

While it is clear that the bi-axial tensile test machine using the cruciform specimen has the advantage of determining the full range of the FLD domain, the equipment design is complex and costly. In ICL, a new testing method was developed by Mohr and Oswald (2007) for testing thin specimens under transverse plane strain conditions. The testing machine, jointly developed by Instron Inc. and the ICL team, can handle in-plane shear, compression/tension and a combination of these loads to generate bi-axial loading conditions. Using this machine, almost the entire strain domain consisting of pure shear, uni-axial tension and plane strain can be achieved, except for the region around the equi-biaxial tension. Therefore, another testing method is required to determine this missing range.

From Table 1, the advantages and disadvantages of the various test methods are discussed. Although cost estimates are not available, a qualitative comparison is performed to determine the most cost effective test method for adoption in ICL, by considering the difficulty levels in developing the equipment and specimen. From the list, the available tests for region in equi-biaxial tension are the Hydraulic Bulge Test, Keeler Punch Stretching Test, Marciniak

Test, Nakazima Test, Hasek Test and the Bi-axial Tensile Test using Cruciform Specimen (in short Cruciform Testing Device). From many previous studies, it is widely acknowledged that friction remains an unknown yet to be effectively characterized and understood. Thus, the list of available tests is greatly reduced to only two options - Hydraulic Bulge Test and Cruciform Testing Device. Further analysis shows that the Cruciform Testing Device is probably the most ideal test for a fresh startup with no existing equipment. However, in this case, being less complex in design of equipment and specimen and thus less costly, the Hydraulic Bulge Test is the preferred choice as a complimentary test method. To further reduce cost and facilitate efficient control of the strain rate during bulging, an innovative system, without the conventional hydraulic pump system, was designed around the existing equipment in the ICL. Optical systems were also employed to determine the geometry of the bulge during the test.

Chapter 3

Design of Experiment

3.1 Existing/Proposed equipping in ICL

Since this is not a fresh startup equipping for a laboratory, it is important to examine the existing equipment and build upon the current capabilities. The ICL is well-equipped with three major pieces of equipment - INSTRON drop tower, MTS machine and ICL self-designed Biaxial Testing machine. The drop tower is used for high strain rate impact experiments while the biaxial testing machine performs the pure shear and plain strain tests. The 200 kN MTS machine is equipped with a load cell for uni-axial tension and compression test. ICL has also acquired a two-camera optical system for tracking multiple locations at the same time. All data from the major equipment and the optical system are fed into the computer system which displays the data on a graphical plot and keeps a log of the measured values.

From Chapter 2, it is proposed to employ the hydraulic bulge test as a complimentary test method. With the existing equipment such as the MTS machine, it is possible to eliminate the need for a complete hydraulic pump system. The proposed equipping is a cylinder plunger attached to the MTS machine to generate a steady and controllable pressure in the hydraulic test chamber for a constant strain rate on the specimen during the bulging process as discussed by Ranta-Eskola (1979). A pressure transducer is used to measure the pressure in the chamber and feed to through the MTS machine for data logging with the computer system. A pressure relief valve is also installed as a safety precaution in the hydraulic piping system rated at 10000 psi (69 MPa).

3.2 Methodology

The approach adopted for the design of the Hydraulic Bulge Test Apparatus is as follows:

Step 1: Identify the range of materials.

Step 2: Perform parametric study between specimen properties such as blank radius, yield / ultimate tensile stress and thickness to determine specimen dimensions.

Step 3: Determine the needed capacity of cylinder plunger such as effective area, pressure rating and volume.

Step 4: Design the hydraulic test chamber including sealing, clamping and localized stress considerations.

Step 5: Design the hydraulic system with safety considerations, data collection and ease of performing experiments.

3.3 Design of apparatus

The common materials used in sheet metal forming are aluminum and steel for manufacturing small items like drink cans, or bigger items like automobiles. Of particular interest, in recent years, is the Advanced High Strength Steels such as the Dual Phase (DP) steel, Transformation Induced Plasticity (TRIP) steel and Complex Phase (CP) steel by the automobile manufacturers. These very high strength steels have ultimate tensile strength ranging from 400 MPa to 1000 MPa as listed by the International Iron and Steel Institute (IIST) (2005). These materials set the upper boundary for the capacity of the new hydraulic bulge test apparatus.

In sheet metal analysis, membrane theory is commonly used to determine the flow stress. It is usually assumed that the thickness-to-length ratio is less than $\frac{1}{20}$, such that the stress and strain field is assumed as uniform throughout the material thickness. Therefore, it is beneficial to have a specimen with a blank radius as large as practicable. However, with a huge radius, it would demand a large amount of hydraulic fluid to fill the bulge and that would require a large volume cylinder plunger. In this case, the cylinder plunger can either be short and fat with a large effective area, but may be beyond the load capacity of the MTS machine, or long and thin with a small effective area, which may be too high to fit into

the MTS loading frame. With these inter-related factors, it is not possible to determine the specimen dimension directly. Therefore, a parametric study using thickness, ultimate tensile strength (UTS) and blank radius as variables was performed over the range of values in Table 2.

Table 2: Specimen design parameters

	Symbol	**Lower Limit**	**Upper Limit**
Thickness (mm)	h_0	1.0	1.8
UTS (MPa)	σ_u	400	1000
Radius (mm)	r_0	25	75

Although hydraulic cylinder plungers can be fabricated according to user requirement, it could drive the cost up significantly. Since one of the considerations of this project was to achieve the objective with the most cost-effective design for the ICL, only off-the-shelf cylinder plungers were considered. From the range of values given in Table 2, the maximum pressure was estimated to occur when the bulge reaches a deflection $w_0 = \frac{r_0}{2}$, and was calculated using Eq. (4).

$$p = 1.19\sigma_u \frac{h_0}{r_0} \tag{4}$$

Depending on the piston's effective area, the corresponding load from the MTS machine was calculated and must fall within the limit of 200 kN. The other consideration was to ensure the bulge volume at point of fracture is less than the volume of the cylinder plunger. Since it is difficult to determine the bulge volume in this case, the maximum volume was estimated as a half sphere, $V = \frac{2}{3}\pi r_0^3$.

Table 3 shows the parametric study highlighting the acceptable dimensions within the load and volume limitations based on three standard models of cylinder plungers of varying capacities. These values are highlighted in the following classification:

Within Limit Above Limit

Alert Limit Limiting Criteria

Table 3: Parametric study for specimen dimensions

			RC-5 Series			RC-10 Series			RC-15 Series		
Case	**Blank radius r_0 (mm)**	**Thickness h (mm)**	**Max Vol of Bulge V (mm^3) (< 148631)**	**Max Pressure at $w_0 = \frac{r_0}{2}$ (GPa)**	**Max Total Force at $w_0 = \frac{r_0}{2}$ ($< 100kN$)**	**Max Vol of Bulge V (mm^3) (< 371167)**	**Max Pressure at $w_0 = \frac{r_0}{2}$ (GPa)**	**Max Total Force at $w_0 = \frac{r_0}{2}$ ($< 100kN$)**	**Max Vol of Bulge V (mm^3) (< 514882)**	**Max Pressure at $w_0 = \frac{r_0}{2}$ (GPa)**	**Max Total Force at $w_0 = \frac{r_0}{2}$ ($< 100kN$)**
A1	75	1.8	883688	0.029	18.23	883688	0.029	32.71	883688	0.029	57.88
A2	70	1.8	718471	0.031	19.53	718471	0.031	35.05	718471	0.031	62.02
A3	65	1.8	575248	0.033	21.03	575248	0.033	37.74	575248	0.033	66.79
A4	60	1.8	452448	0.036	22.78	452448	0.036	40.89	452448	0.036	72.35
A5	55	1.8	348500	0.039	24.86	348500	0.039	44.61	348500	0.039	78.93
A6	50	1.8	261833	0.043	27.34	261833	0.043	49.07	261833	0.043	86.82
A7	45	1.8	190877	0.048	30.38	190877	0.048	54.52	190877	0.048	96.47
A8	40	1.8	134059	0.054	34.18	134059	0.054	61.33	134059	0.054	108.53
A9	35	1.8	89809	0.061	39.06	89809	0.061	70.10	89809	0.061	124.03
A10	30	1.8	56556	0.071	45.57	56556	0.071	81.78	56556	0.071	144.70
A11	25	1.8	32729	0.086	54.68	32729	0.086	98.14	32729	0.086	173.64
B1	75	1.6	883688	0.025	16.20	883688	0.025	29.08	883688	0.025	51.45
B2	70	1.6	718471	0.027	17.36	718471	0.027	31.15	718471	0.027	55.13
B3	65	1.6	575248	0.029	18.69	575248	0.029	33.55	575248	0.029	59.37
B4	60	1.6	452448	0.032	20.25	452448	0.032	36.35	452448	0.032	64.31
B5	55	1.6	348500	0.035	22.09	348500	0.035	39.65	348500	0.035	70.16
B6	50	1.6	261833	0.038	24.30	261833	0.038	43.62	261833	0.038	77.18
B7	45	1.6	190877	0.042	27.00	190877	0.042	48.46	190877	0.042	85.75
B8	40	1.6	134059	0.048	30.38	134059	0.048	54.52	134059	0.048	96.47
B9	35	1.6	89809	0.054	34.72	89809	0.054	62.31	89809	0.054	110.25
B10	30	1.6	56556	0.063	40.50	56556	0.063	72.69	56556	0.063	128.63
B11	25	1.6	32729	0.076	48.61	32729	0.076	87.23	32729	0.076	154.35
C1	75	1.4	883688	0.022	14.18	883688	0.022	25.44	883688	0.022	45.02
C2	70	1.4	718471	0.024	15.19	718471	0.024	27.26	718471	0.024	48.23
C3	65	1.4	575248	0.026	16.36	575248	0.026	29.36	575248	0.026	51.94
C4	60	1.4	452448	0.028	17.72	452448	0.028	31.80	452448	0.028	56.27
C5	55	1.4	348500	0.030	19.33	348500	0.030	34.69	348500	0.030	61.39
C6	50	1.4	261833	0.033	21.27	261833	0.033	38.16	261833	0.033	67.53
C7	45	1.4	190877	0.037	23.63	190877	0.037	42.40	190877	0.037	75.03
C8	40	1.4	134059	0.042	26.58	134059	0.042	47.70	134059	0.042	84.41
C9	35	1.4	89809	0.048	30.38	89809	0.048	54.52	89809	0.048	96.47
C10	30	1.4	56556	0.056	35.44	56556	0.056	63.61	56556	0.056	112.55
C11	25	1.4	32729	0.067	42.53	32729	0.067	76.33	32729	0.067	135.06
D1	75	1.2	883688	0.019	12.15	883688	0.019	21.81	883688	0.019	38.59
D2	70	1.2	718471	0.020	13.02	718471	0.020	23.37	718471	0.020	41.34
D3	65	1.2	575248	0.022	14.02	575248	0.022	25.16	575248	0.022	44.52
D4	60	1.2	452448	0.024	15.19	452448	0.024	27.26	452448	0.024	48.23
D5	55	1.2	348500	0.026	16.57	348500	0.026	29.74	348500	0.026	52.62

continued on next page

Table 3 – continued from previous page

Case	Blank radius r_0 (mm)	Thickness h (mm)	Max Vol of Bulge V (mm^3) (< 148631)	Max Pressure at $w_0 = \frac{r_0}{2}$ (GPa)	Max Total Force at $w_0 = \frac{r_0}{2}$ ($< 100kN$)	Max Vol of Bulge V (mm^3) (< 371167)	Max Pressure at $w_0 = \frac{r_0}{2}$ (GPa)	Max Total Force at $w_0 = \frac{r_0}{2}$ ($< 100kN$)	Max Vol of Bulge V (mm^3) (< 514882)	Max Pressure at $w_0 = \frac{r_0}{2}$ (GPa)	Max Total Force at $w_0 = \frac{r_0}{2}$ ($< 100kN$)
D6	50	1.2	261833	0.029	18.23	261833	0.029	32.71	261833	0.029	57.88
D7	45	1.2	190877	0.032	20.25	190877	0.032	36.35	190877	0.032	64.31
D8	40	1.2	134059	0.036	22.78	134059	0.036	40.89	134059	0.036	72.35
D9	35	1.2	89809	0.041	26.04	89809	0.041	46.73	89809	0.041	82.69
D10	30	1.2	56556	0.048	30.38	56556	0.048	54.52	56556	0.048	96.47
D11	25	1.2	32729	0.057	36.45	32729	0.057	65.42	32729	0.057	115.76
E1	75	1.0	883688	0.016	10.13	883688	0.016	18.17	883688	0.016	32.16
E2	70	1.0	718471	0.017	10.85	718471	0.017	19.47	718471	0.017	34.45
E3	65	1.0	575248	0.018	11.68	575248	0.018	20.97	575248	0.018	37.10
E4	60	1.0	452448	0.020	12.66	452448	0.020	22.72	452448	0.020	40.20
E5	55	1.0	348500	0.022	13.81	348500	0.022	24.78	348500	0.022	43.85
E6	50	1.0	261833	0.024	15.19	261833	0.024	27.26	261833	0.024	48.23
E7	45	1.0	190877	0.026	16.88	190877	0.026	30.29	190877	0.026	53.59
E8	40	1.0	134059	0.030	18.99	134059	0.030	34.07	134059	0.030	60.29
E9	35	1.0	89809	0.034	21.70	89809	0.034	38.94	89809	0.034	68.91
E10	30	1.0	56556	0.040	25.32	56556	0.040	45.43	56556	0.040	80.39
E11	25	1.0	32729	0.048	30.38	32729	0.048	54.52	32729	0.048	96.47

From the parametric study, it was observed that the RC-10 Series is applicable over the largest range of specimen dimension. A convenient blank radius is $r_0 = 50mm$. The cylinder plunger RC-108 was chosen to provide the fluid pressure to the test chamber.

The other aspects of the design involve the sealing, clamping and localized stress considerations for the test chamber. For a specimen with blank radius $r_0 = 50mm$, the maximum pressure is 43 MPa or 6235 psi. Thus, the test chamber was rated to 10,000 psi (69 MPa) giving a safety factor of at least 1.6. The other consideration associated with pressure rating is the seal design. Two specific types of seal designs were explored - static axial seal and static crush seal. Although both seal designs were applicable, the static axial seal design was preferred for its simplicity and reusability. Figure 3 shows the static axial seal design. The seal design follows the AS568-159 design guidelines for internal pressure with the following parameters:

$$\begin{aligned} \text{Diameter, A} &= 5.188 \text{ inch or } 131.8 \text{ mm} \\ \text{Gland Width, G} &= 0.17 \text{ inch or } 4.3 \text{ mm} \end{aligned}$$

Gland Depth, H = 0.075 inch or 1.9 mm

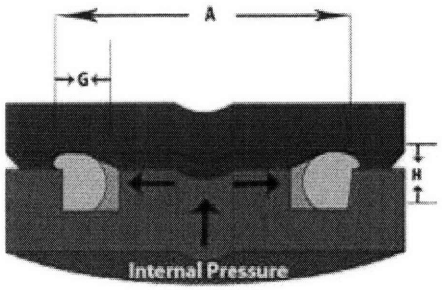

Figure 3: Static axial seal design (taken from Columbia Engineered Rubber, Inc. http://www.columbiaerd.com/gland_design.html)

The clamp design used 12 grade 8 bolts which have a proof load of 120,000 psi (827 MPa) each. There was sufficient holding force and the 12 bolts provided even load distribution and prevented flexure of the flange which would have affected the accuracy of the test. An all-round draw bead was also used to prevent slippage of the test specimen during the test. The hard corner on the opening of the circular die created localized stress and a fillet with radius $r_f = 3$ mm was applied to this design, as shown in Figure 4.

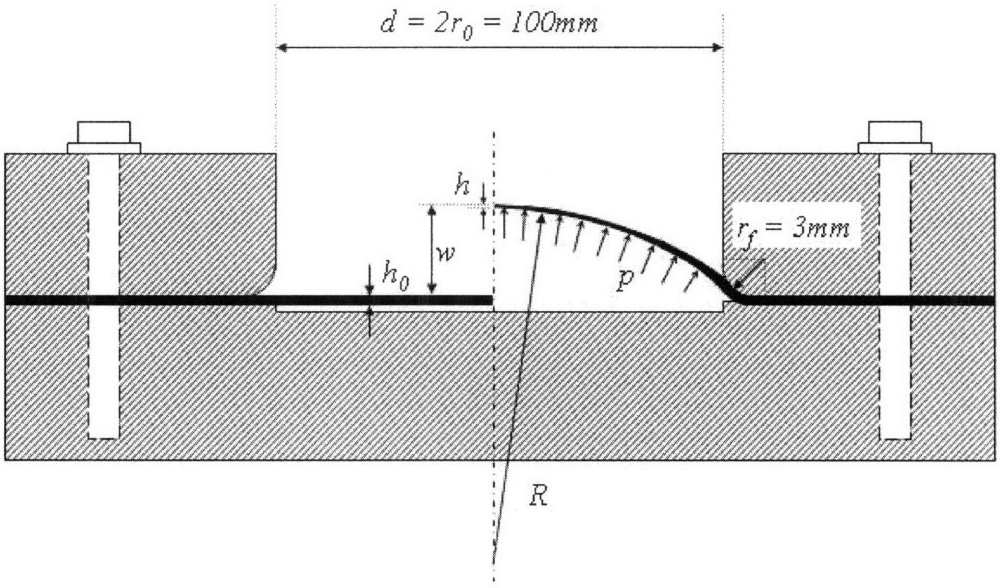

Figure 4: Geometry of the test chamber

The test chamber formed part of the hydraulic system as shown in the hydraulic schematic diagram in Figure 5. As a safety precaution, a pressure relief valve was installed between the cylinder plunger (where the pressure was applied) and the inlet valve to the test chamber to prevent over-pressure which could damage the apparatus and injure the operator. Although a pressure gauge was installed for easy observation of the pressure in the test chamber, a more accurate value was recorded using a pressure transducer with an output connected to a computer system which logged the pressure vs time curve. At the same time, the load cell on the MTS machine also provided the force which could be used for the verification of pressure values.

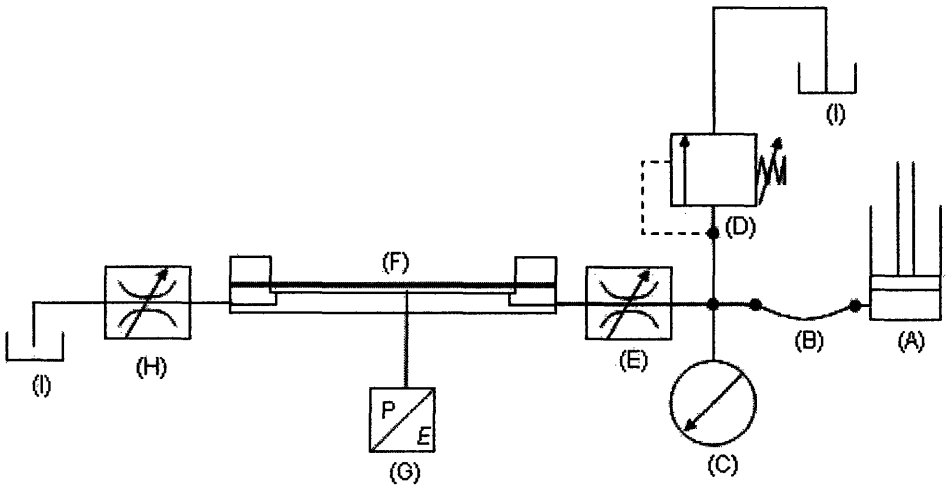

Figure 5: Hydraulic Schematic Diagram

A flexible hydraulic hose was used so that the test chamber could be placed at a more spacious location away from the MTS machine. This was to allow the positioning of the apparatus for the optical recording of the bulge. There were two needle valves – inlet and outlet valves. These valves were located at their respective locations mainly for the filling process. As there was no hydraulic pump to fill the cylinder plunger with fluid, the entire hydraulic system had to be filled in stages to prevent any air pockets from residing in the system during the test. The list of components is in Table 4. A detailed description of the filling process is explained in Section 3.4.

Table 4: List of Components

	Component	**Model**	**Qty**
A1	Hydraulic Cylinder	RC-108	1
A2	Quick Coupler	CR-400	1
A3	Base Plate	JBI-10	1
B1	Flexible Hose	H-9203	1
B2	Cross Fitting	FZ-1613	1
C1	Pressure Gauge	G-2535	1
C2	Bushing	FZ-1630	1
D1	Pressure Relief Valve w Return Line	V-152	1
D2	Hex Nipple	FZ-1617	1
E1	Needle Valve, Inlet	V-82	1
E2	Quick Coupler	McMaster Part# 53455K55 Part# 53455K28	1
E3	Hex Nipple	FZ-1617	1
E4	Bushing	FZ-1630	1
E5	Hex Nipple	FZ-1608	1
F	Test Chamber	Custom Made	1
G	Pressure Transducer	GEMS 3100	1
H1	Needle Valve, Outlet	V-82	1
H2	Bushing	FZ-1630	1
H3	Hex Nipple	FZ-1608	1
I	Hydraulic Tank w Hydraulic Oil	HF-101	1

All components (under pressure) rated up to 10,000psi

The test chamber had an enclosure to contain any spillage when the specimen ruptured and the groove around the enclosure allowed the hydraulic fluid to flow away. As an optical recording system was to be used in this design, two cameras were used to generate the stereo picture, as shown in Figure 6.

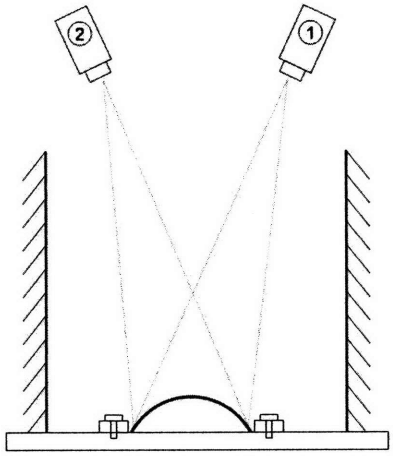

Figure 6: Optical recording system arrangement

3.4 Experimental procedures

To achieve accurate results from the experiments, the following steps were followed:

a. Specimen preparation

b. System calibration

c. Pre-test preparation

d. Testing process

e. Post-test maintenance

3.4.1 Specimen preparation

The test sheet material was first cut into a circular disc with diameter 170mm using the waterjet cutting tool. 12 holes were also cut out to fit the holding bolts in the dies. Figure 7 shows the layout and dimensions of the specimen. The specimen was subsequently spray

painted with a white base and random black fine dots across the surface for the optical measuring system.

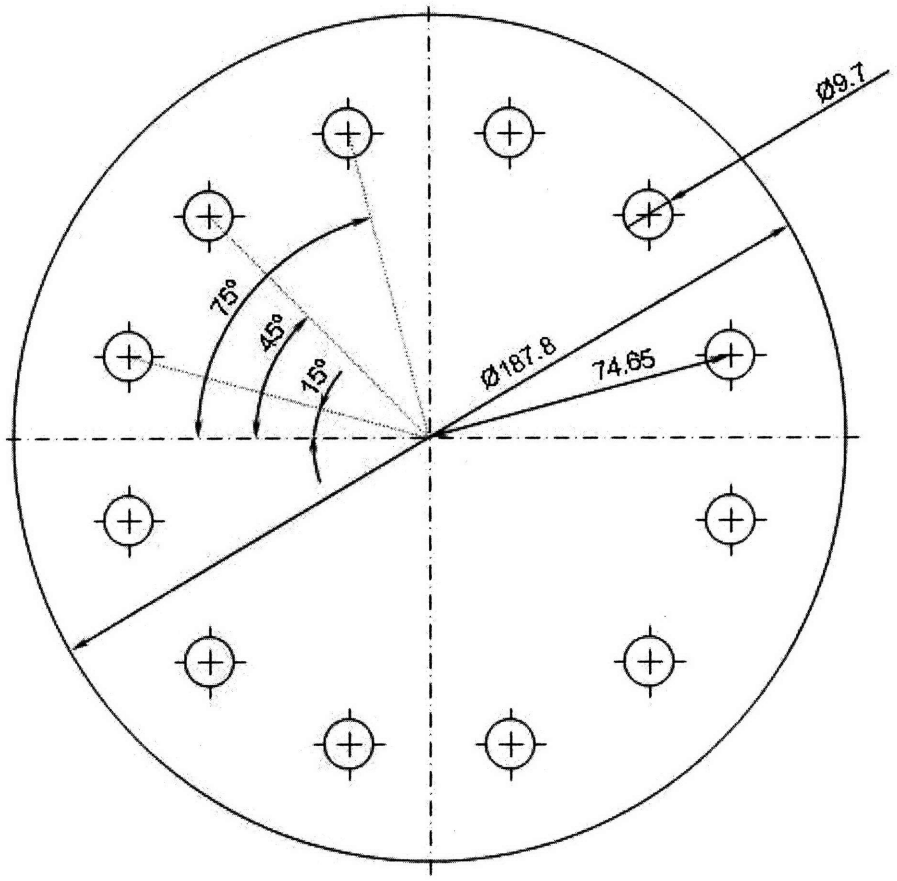

Figure 7: Layout and dimensions of test specimen

3.4.2 System calibration

The pressure transducer and optical measuring system had to be calibrated before the conduct of experiment. The pressure transducer was first fixed directly to the cylinder plunger with the plunger arm fully extended and connected to the MTS load cell. The load increased as the MTS loading frame depressed the plunger arm and the voltage output from the pressure transducer was measured. The pressure in the cylinder was calculated using the relationship in Eq. (5) and the pressure-voltage calibration curve was determined.

$$p = \frac{F}{A} \tag{5}$$

where

p : pressure in the cylinder

F : force data from the load cell

$A = 1145mm^2$: effective area of the plunger

The entire experiment was setup before performing the calibration of the optical measuring system. The two-camera optical measuring system was calibrated using the Vic-3D software and calibration target (size: 10x13 - 2.8mm). The software then determined the positions of the two cameras and was thus able to calculate the spatial dimensions of the bulge during the test.

3.4.3 Pre-test preparation

The pre-test preparation involved filling the hydraulic system in stages to eliminate air gaps in the hydraulic system which may affect the pressure in the test chamber. The cylinder plunger was placed in the horizontal position with the hydraulic hose and fixtures attached up to the inlet valve as shown in the photograph in Figure 8. The hydraulic oil was then fed through the inlet valve slowly to the brim and the valve was shut.

The rest of the test apparatus was then connected without the specimen. The inlet valve was opened and the test chamber was filled slowly to brim as shown in the photograph in Figure 9.

The specimen was then attached and the die was bolted down. The outlet valve was opened and the cylinder plunger was depressed using the MTS loading frame until a steady flow was achieved. Then, the MTS loading frame was stopped and the outlet valve shut off at the same time, as shown in the photograph in Figure 10. This process got rid of most, if not all, of the air pockets in the system.

The final experiment setup is as shown in Figure 11.

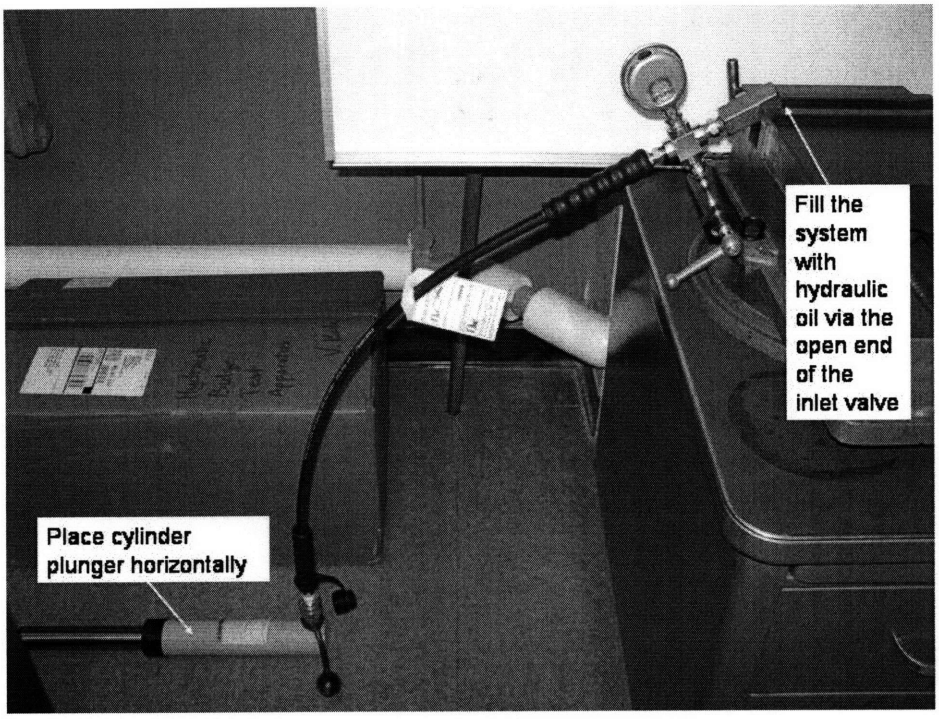

Figure 8: Pre-test preparation (Step 1)

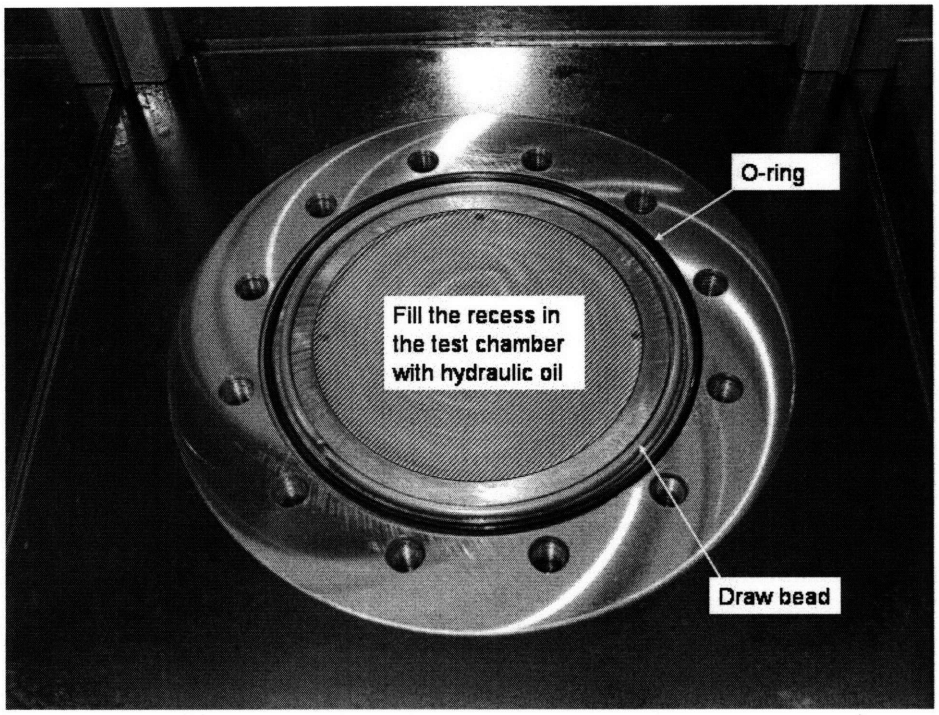

Figure 9: Pre-test preparation (Step 2)

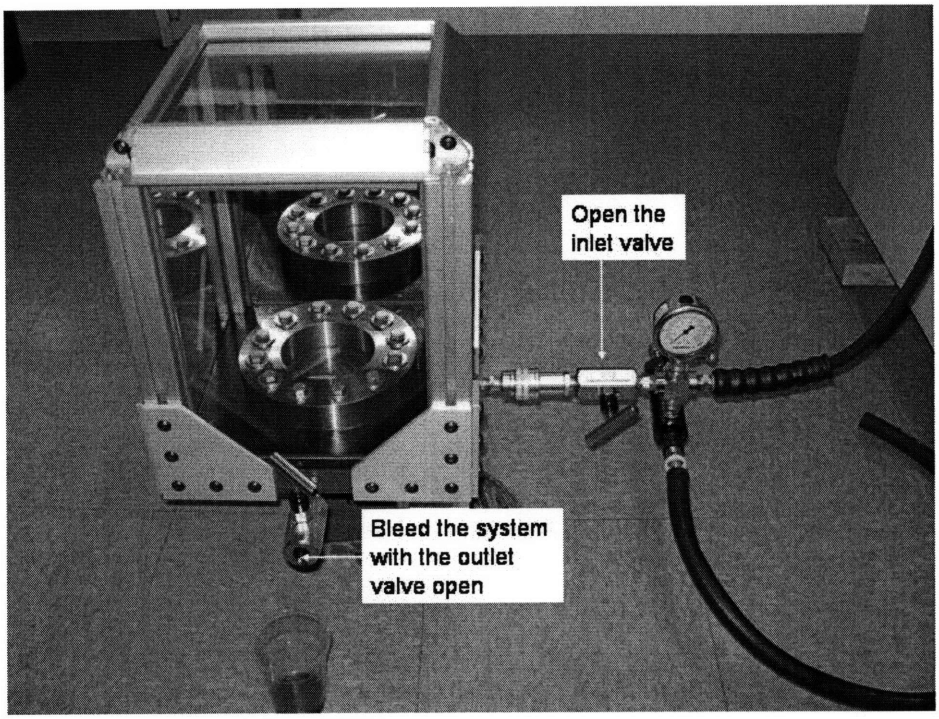

Figure 10: Pre-test preparation (Step 3)

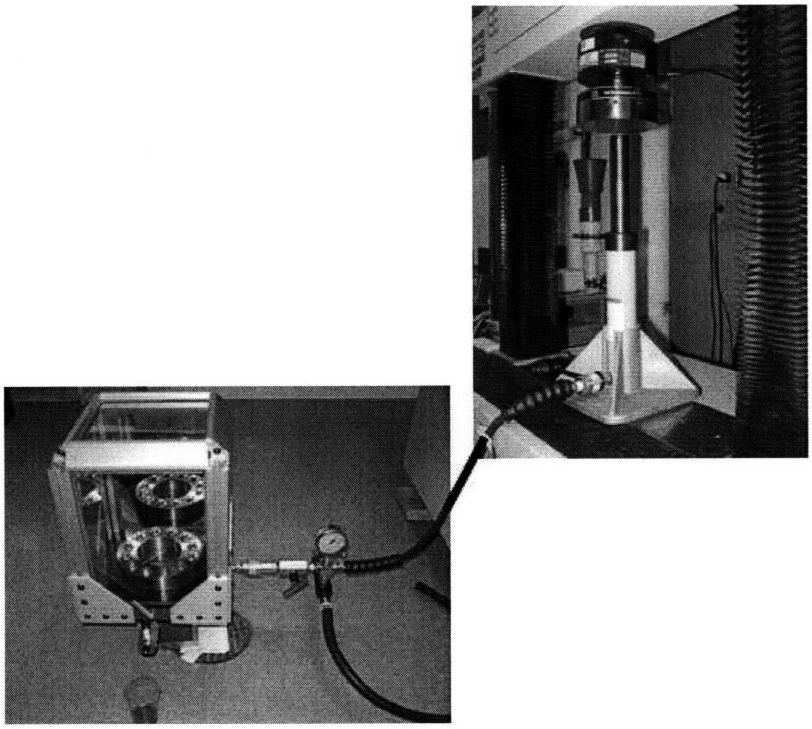

Figure 11: Experiment setup

3.4.4 Testing process

The output cables from the load cell and pressure transducer were connected to the MTS machine for data acquisition via the computer system. The optical displacement measurements from the optical measuring system were also connected to the computer system for recording and visualization of the displacement for subsequent strain calculations.

The cylinder plunger was connected to the load cell and the MTS loading frame was set to move at a constant rate of 5mm/min using the control system. As the pressure during fracture of the specimen could be relatively high, care was taken to constantly monitor the pressure gauge reading and pressure transducer value during the entire testing process. The MTS load and data acquisition was stopped immediately when the specimen ruptured.

3.4.5 Post-test maintenance

Upon completion of the test, the outlet valve was opened to drain the hydraulic fluid from the test chamber. At the same time, any spillage in the enclosure was drained off and discarded. It was important to ensure that the hydraulic oil in the enclosure was not recycled as there could be tiny metal chips from the fracture which may impinge and deteriorate the seals in the hydraulic system. It was not necessary to clean all the surfaces as the hydraulic oil would act as a protective layer to prevent rust. The specimen was removed and cleaned for further observations and analysis. The inlet valve was opened to drain off all hydraulic oil in the cylinder and other parts of the system back into the hydraulic reservoir.

3.5 Data processing

From the experiment, three data sets were recorded from the MTS load cell, pressure transducer and optical measuring device. The MTS load cell data acted as a counter-check for the pressure transducer data to confirm the internal pressure in the bulge. With the calibrated voltage output, the pressure acting on the bulge could be calculated. The optical measuring device was only required to record a quarter of the specimen due to symmetry. This design also allowed observations of anisotropy, if any, although not required for the analysis of equi-biaxial tension which occurs at the top of the dome. Therefore, the area observed was limited to the top of the dome. From the optical recordings, two fixed points were defined, one at the top of the dome and the other slightly displaced from the former in order to calculate

the radius of curvature at the top. The analysis is discussed in the next chapter. Strain was also calculated from the bulge displacement which was then used to determine the dome height. From which, the equivalent stress could be determined using the three measured or calculated parameters - internal pressure, radius of curvature and dome height.

In fact, with all three data sets recorded in the same time series, the entire bulging process could be determined. The results could be used for validating the trajectory of the particles on the bulge surface to better understand the biaxial stress-strain relationships other than the equi-biaxial range which occurs only at the top of the dome.

Chapter 4

Analysis and Results

4.1 Theoretical Analysis

4.1.1 Analytical approximation

The membrane theory is used to determine the flow stress in the hydraulic bulge test. For an axi-symmetric shell under uniform pressure (Figure 12),

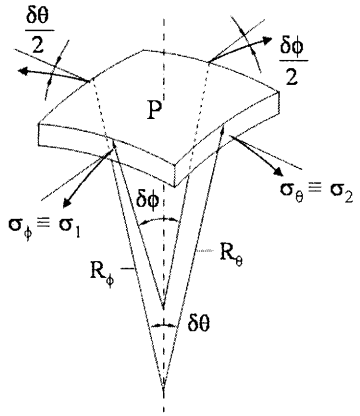

Figure 12: Equilibrium of stresses for a membrane element

the in-plane stresses, pressure and geometry form a relationship:

$$\frac{\sigma_1}{R_\phi} + \frac{\sigma_2}{R_\theta} = \frac{p}{h} \tag{6}$$

where

σ_1, σ_2 : principal stresses on the membrane

R_ϕ, R_θ : corresponding radii of the curved surface

p : uniform pressure

h : membrane thickness at the top of the dome

Assuming isotropic material, the in-plane stresses are equal at the center of the spherical shell. Thus $\sigma_1 = \sigma_2 = \sigma_m$, and $R_\phi = R_\theta = R$, giving a simplified relationship:

$$\sigma_1 = \sigma_2 = \sigma_m = \frac{pR}{2h} \tag{7}$$

From Ugural and Fenster (1995), the maximum bending stress, σ_b, in the membrane is derived:

$$\sigma_b = \frac{p}{4} \tag{8}$$

By comparing σ_m and σ_b,

$$\frac{\sigma_m}{\sigma_b} = \frac{2R}{h} \tag{9}$$

for a circular membrane with very small thickness-to-radius ratio, it is concluded that the in-plane stress is much larger than the bending stress ($\sigma_m \gg \sigma_b$), such that the bending stress in the membrane can be omitted from this analysis with negligible error. It is also assumed that the normal (through-thickness) stress component is negligible in the membrane theory, i.e. $\sigma_3 = 0$. Therefore, the equivalent stress,

$$\begin{aligned} \bar{\sigma} &= \sqrt{\frac{1}{2}\left[(\sigma_1 - \sigma_2)^2 + (\sigma_2 - \sigma_3)^2 + (\sigma_3 - \sigma_1)^2\right]} \\ &= \sigma_m \\ &= \frac{pR}{2h} \end{aligned} \tag{10}$$

Assuming material incompressibility, the sum of the principal strains is zero.

$$\varepsilon_1 + \varepsilon_2 + \varepsilon_3 = 0 \tag{11}$$

where

$\varepsilon_1, \varepsilon_2$: principal strains on the membrane

ε_3 : normal (through-thickness) strain

At the top of the dome, the in-plane strains are equal, $\varepsilon_1 = \varepsilon_2 = \varepsilon_m$. The strain magnitude can be calculated based on geometrical measurements (Figure 13) as shown in Eq. (12).

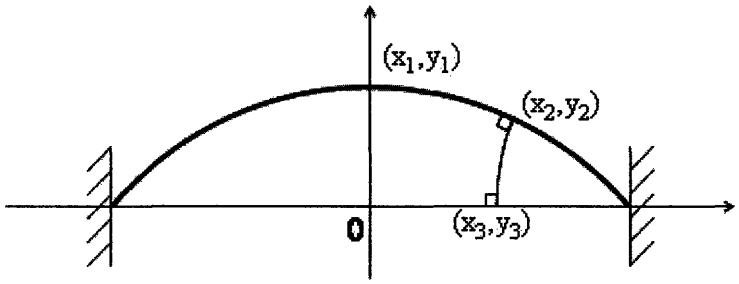

Figure 13: Geometrical construction for determining strain at top of dome from measurements

$$\varepsilon_1 = \varepsilon_2 = \varepsilon_m = \ln\left(\frac{x_2 - x_1}{x_3 - x_1}\right) \tag{12}$$

where (x_1, y_1) is the point at the top of the dome; (x_2, y_2) is the same point on the dome surface as (x_3, y_3) after bulging. This point is chosen very close to (x_1, y_1) so that the curvature of the dome is negligible.

Similarly, the normal (through-thickness) strain ε_3 can be calculated from the geometry.

$$\varepsilon_3 = \ln\left(\frac{h}{h_0}\right) \tag{13}$$

where h_0 is the initial thickness of the sheet specimen. Therefore, the equivalent strain is given by

$$\begin{aligned} \bar{\varepsilon} &= \sqrt{\frac{2}{9}\left[(\varepsilon_1 - \varepsilon_2)^2 + (\varepsilon_2 - \varepsilon_3)^2 + (\varepsilon_3 - \varepsilon_1)^2\right]} \\ &= \ln\left(\frac{h_0}{h}\right) \end{aligned} \tag{14}$$

From Eq. (10), the flow stress of the material can be determined from the three variables, pressure p, radius of curvature R, and thickness at the top of the dome h. There are two ways of determining each of these three values. The pressure p can be measured using the calibrated pressure transducer data or calculated from the force in the load cell over the effective area of the piston. The former method is preferred as the pressure transducer measures the pressure in the bulge directly, negating any possible errors such as leakage in the hydraulic system. However, the latter method acts as an operability check of the pressure transducer and also possible leakages in the system so as to perform any corrective maintenance.

For the other variables, R and h, the two ways are experimental measurements and theoretical approximations. The former method employs the dual-camera optical system to record and reconstruct the bulge geometry near the top of the dome. This gives a great advantage as R and h can be calculated through the geometrical relationships (Figure 14) as shown in Eq. (15) and (17).

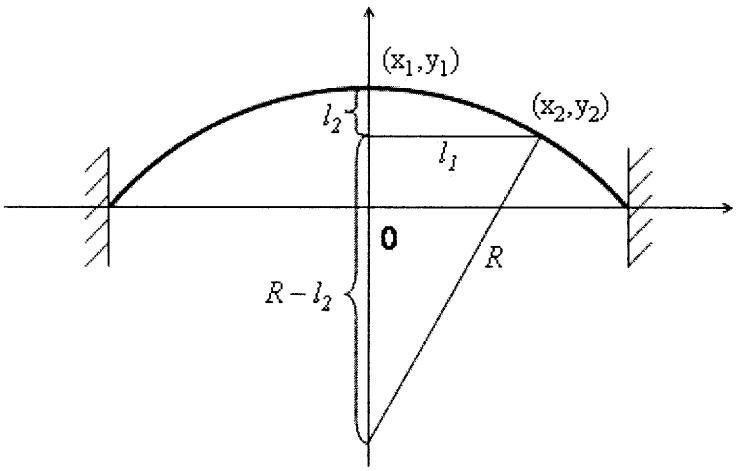

Figure 14: Geometrical construction for determining radius of curvature from measurements

Using Pythagoras' Theorem,

$$\begin{aligned} R^2 &= (R - l_2)^2 + l_1^2 \\ R &= \frac{l_1^2 + l_2^2}{2l_2} \\ &= \frac{(x_2 - x_1)^2 + (y_1 - y_2)^2}{2(y_1 - y_2)} \end{aligned} \tag{15}$$

From the condition of incompressibility in Eq. (11),

$$\varepsilon_3 = -(\varepsilon_1 + \varepsilon_2) \tag{16}$$

Substituting Eq. (12) and (13) into Eq. (16)

$$\begin{aligned} \ln\left(\frac{h}{h_0}\right) &= -2\ln\left(\frac{x_2 - x_1}{x_3 - x_1}\right) \\ \frac{h}{h_0} &= \left(\frac{x_2 - x_1}{x_3 - x_1}\right)^{-2} \\ h &= \left(\frac{x_3 - x_1}{x_2 - x_1}\right)^{2} h_0 \end{aligned} \tag{17}$$

The alternative method of determining the radius of curvature R is by making the assumption that the dome is spherical in shape and relying on geometrical relationship between the measured dome height w and the radius of curvature R while taking into account the fillet at the clamped edge. This relationship is as shown by Gutscher et al (2004) in Eq. (18), and Panknin (1959) and Gologranc (1975) has verified the assumption to be in good agreement with experimental data for a shallow bulge up to $\frac{w_0}{r_0} = 0.56$, where w_0 is the maximum dome height, r_0 is the blank radius and r_f is the fillet radius.[1]

$$R = \frac{(r_0 + r_f)^2 + w_0^2 - 2r_f w_0}{2w_0} \tag{18}$$

The other variable, sheet thickness h at the top of the dome, can be determined using Eq. (19) derived by Chakrabarty and Alexander (1970) with the assumption that the strain hardening index n plays a part in the strain distribution.[1]

$$h = h_0 \left[\frac{1}{1 + (\frac{w_0}{r_0})^2}\right]^{2-n} \tag{19}$$

The uni-axial tensile test is first performed to determine the initial values of material strength coefficient K and strain hardening index n in the power law equation:

$$\sigma = K\varepsilon^n \tag{20}$$

[1]Derivation can be found in Appendix C.

Using this initial n value, p, R and h are substituted into Eq. (10) and (14) to calculate the initial values of σ and ε. Since K is independent of variables h and R, the new n value can be calculated using Eq. (20). Through an iterative process, the n value converges to n_{final} value which is used to calculate the actual stress σ.

4.1.2 Necking and Fracture

In the hydraulic bulge test for a ductile material, it is likely that necking will occur before fracture. As the onset of necking is an undesirable state in sheet metal forming, it is useful to be able to determine this value. Bressan and Williams (1982) proposed a shear instability criterion to predict local necking in sheet metal deformation, allowing the prediction of in-plane strain ε_r for the equibiaxial test at the center of the circular membrane:

$$\varepsilon_r = \frac{2\alpha}{BD^{\frac{m-1}{m}}}\left[\left(\frac{A}{A_p}\right)^{\frac{1}{nm}}\left(\frac{3}{\sqrt{2}}C\right)^{\frac{1}{n}} Z_n - \varepsilon_0\right] \tag{21}$$

where

$$\begin{aligned}
A &= [(1+2R)(1-X)^m + (1+X)^m] \\
B &= [2(1+R)]^{\frac{1}{m}} \\
C &= \frac{\sqrt{2(2\alpha+1)}}{6\sqrt{\alpha^2+\alpha}} \\
D &= \left[\left(\tfrac{1}{1+2R}\right)^{\frac{1}{m-1}}(\alpha-1)^{\frac{m}{m-1}} + (1+\alpha)^{\frac{m}{m-1}}\right] \\
X &= \frac{1-\left[\frac{\alpha-1}{(\alpha+1)(1+2R)}\right]^{\frac{1}{m-1}}}{1+\left[\frac{\alpha-1}{(\alpha+1)(1+2R)}\right]^{\frac{1}{m-1}}} \\
Z &= \tfrac{1}{2}\left[\tfrac{2(1+R)}{1+2R}\right]^{\frac{1}{m}}\left[1+(1+2R)^{\frac{1}{m-1}}\right]^{\frac{m-1}{m}} \\
A_p &= \left[(1+2R)+(1+2R)^{\frac{m}{m-1}}\right]\left[\frac{2}{(1+2R)^{\frac{1}{m-1}}+1}\right]^m
\end{aligned}$$

$\alpha = -\frac{1+R}{R}$: ratio of principal strain increments

$R = \frac{\varepsilon_w}{\varepsilon_t}$: strain ratio of sheet material (measure of anisotropy)

ε_w : strain in the wide direction in a tensile test

ε_t : strain in the thickness direction in a tensile test

n : work hardening exponent

m : modified Hill yield criterion exponent for$R < 1$

ε_0 : initial prestrain (if any)

For the isotropic material, ($R = 1$), the through-thickness strain ε_m at the top of the dome is obtained as a special case of Eq. (21):

$$\varepsilon_n = -2\varepsilon_r = \frac{2n}{\left(\frac{\sqrt{2}}{3}\right)^{\frac{1}{n}} (\sqrt{3})^{\frac{1-n}{n}}} - \varepsilon_0 \tag{22}$$

From Eq. (22), assuming zero prestrain ($\varepsilon_0 = 0$), the thickness h can be determined. This provides an estimate of the onset of local necking.

$$\begin{aligned} \ln \frac{h}{h_0} &= \frac{2n}{\left(\frac{\sqrt{2}}{3}\right)^{\frac{1}{n}} (\sqrt{3})^{\frac{1-n}{n}}} \\ h &= h_0 \exp\left[\frac{2n}{\left(\frac{\sqrt{2}}{3}\right)^{\frac{1}{n}} (\sqrt{3})^{\frac{1-n}{n}}}\right] \end{aligned} \tag{23}$$

For a more brittle material, it is possible that fracture occurs before necking. The hydraulic bulge test serves as a means to validate the B-W fracture criterion in Eq. (1) in the range of equi-biaxial tension. This criterion can then be used to predict the point of fracture in the FFLD.

4.2 Numerical Analysis

The material used in this numerical analysis is DP450 from US Steels. The sheet material was previously tested using uni-axial tensile test with the material properties in Table 5. The stress-strain curve is shown in Figure 15.

Table 5: Uni-axial tensile test for DP450

	Uni-axial Tensile Test
Yield Stress, σ_y	320 MPa
Ultimate Tensile Stress, σ_u	636 MPa
Material Strength Coefficient, K	744
Strain Hardening Index, n	0.14

Using the material properties from the uni-axial tensile test, the finite element model was constructed. The FEM software used is Abaqus with input values given in Table 6 and the

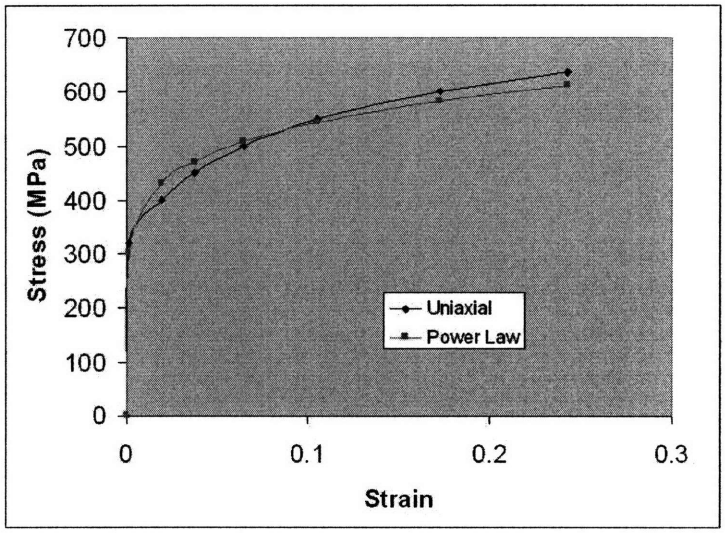

Figure 15: Stress-strain curve from uni-axial tensile test

analysis output as shown in Figures 16 - 20.

Table 6: Input to FEM analysis (Abaqus)

Parameters	**Values**							
Mass Density	7.8×10^{-9}kg/mm^3							
Young's Modulus	200000 MPa							
Poisson's Ratio	0.3							
Yield Stress	320	400	450	500	550	600	636	1026
Plastic Strain	0.000	0.018	0.036	0.063	0.104	0.171	0.241	1.000
Nlgeom	ON							
Load Distribution	Uniform							
Load Magnitude	40 MPa							
Load Amplitude	Ramp (0 to 1)							
Boundary Condition	Clamped ($U_i = 0$)							
Mesh Global Size	3							
Curvature Control Deviation Factor	0.1							
Element Shape	Hex							
Element Control	Reduced Integration							
Kinematic Split	Average Strain							
Second Order Accuracy	No							
Distortion Control	Default							
Hourglass Control	Default							

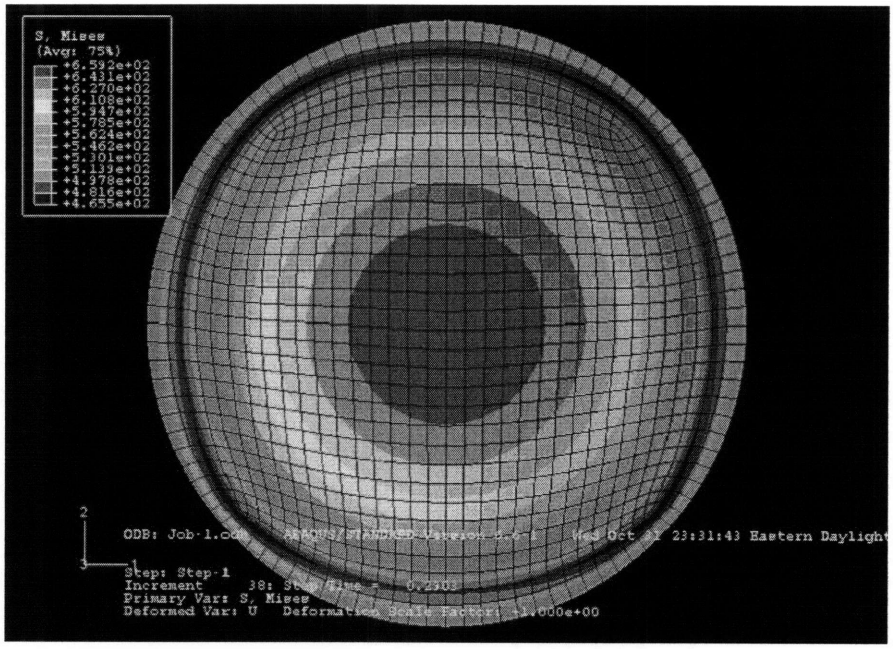

Figure 16: Stress distribution over the dome surface

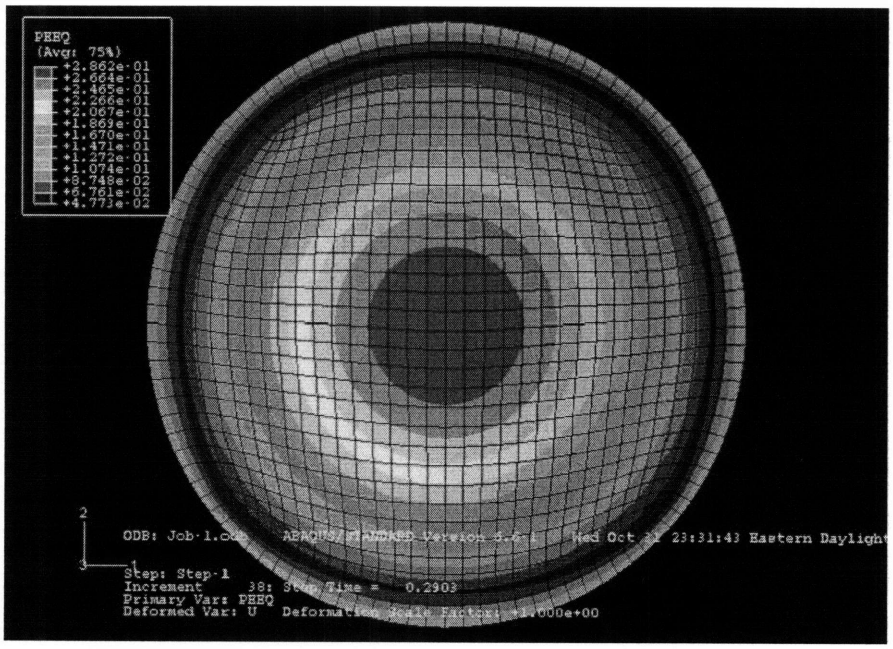

Figure 17: Strain distribution over the dome surface

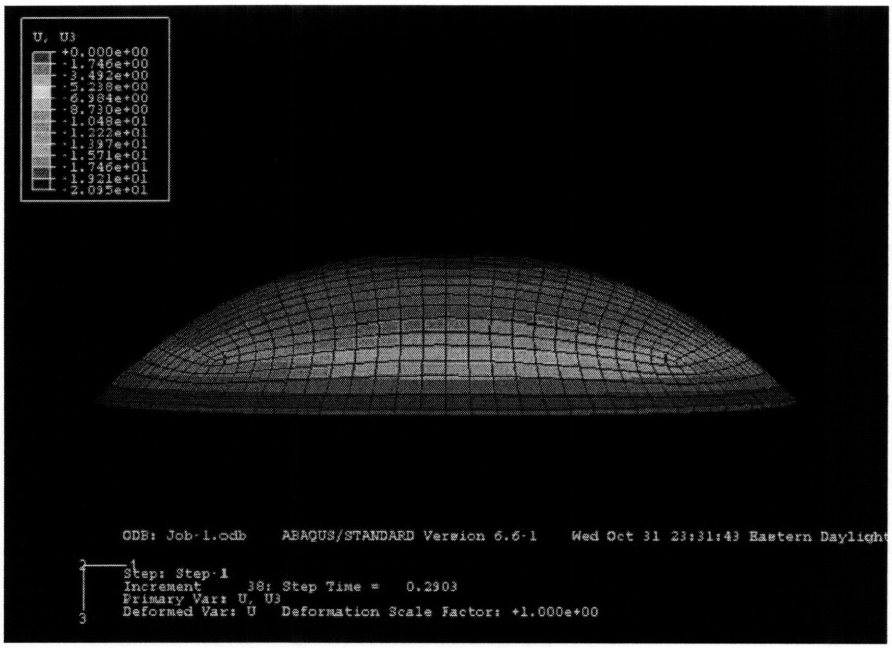

Figure 18: Vertical displacement of the dome surface

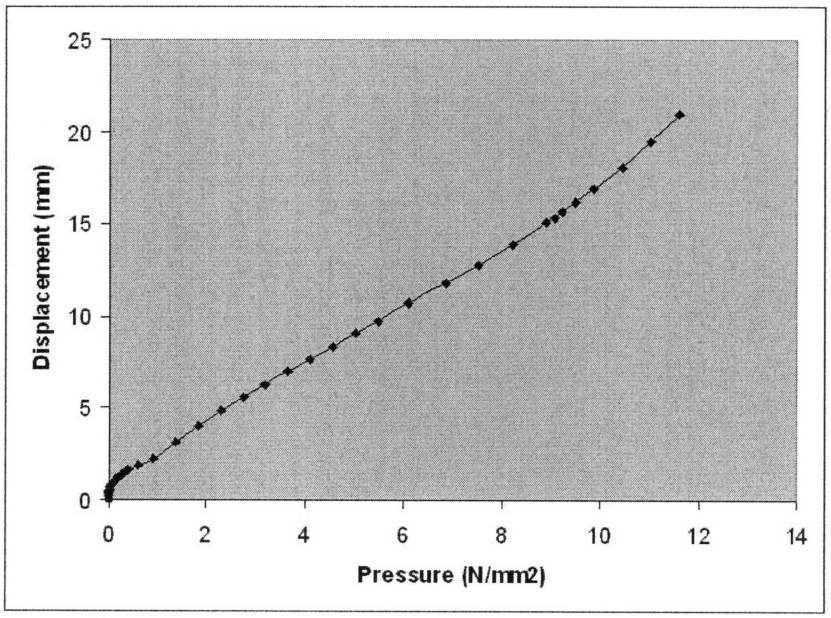

Figure 19: Pressure-displacement relationship at the top of the dome (equi-biaxial tension)

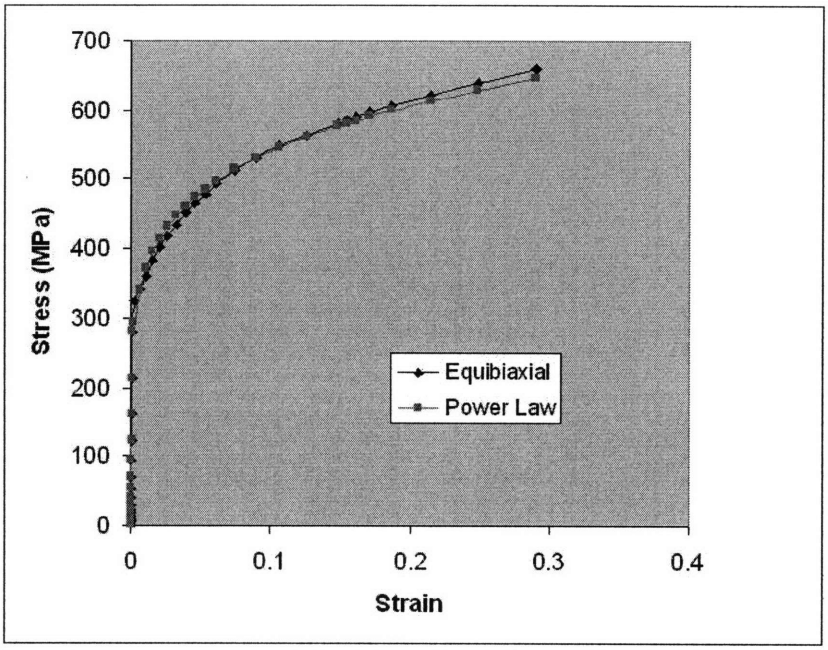

Figure 20: Stress-strain relationship at the top of the dome (equi-biaxial tension)

4.3 Results

The experimental results for galvanized steel are as shown below. Two experiments were performed to demonstrate the effectiveness of this equipment.

In the first experiment, the circular die did not have a fillet on the inner diameter. The specimen developed a smooth bulge as the internal pressure increased. There were no noticeable leaks and pressure was able to build up gradually until the point of fracture. The pressure gauge was also working properly, giving a quick indicator of the pressure in the system. The pictures of the specimen are shown in Figure 21.

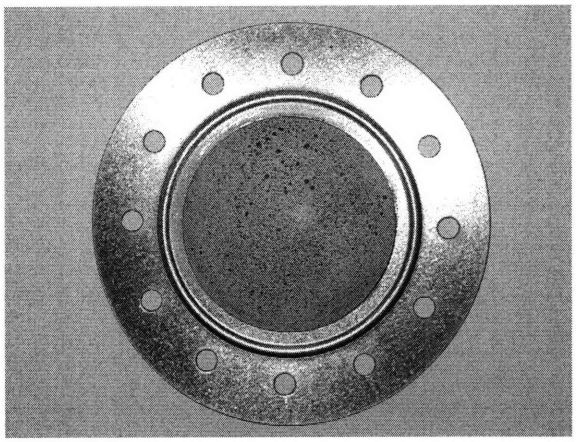

(a) Plan view of the bulge

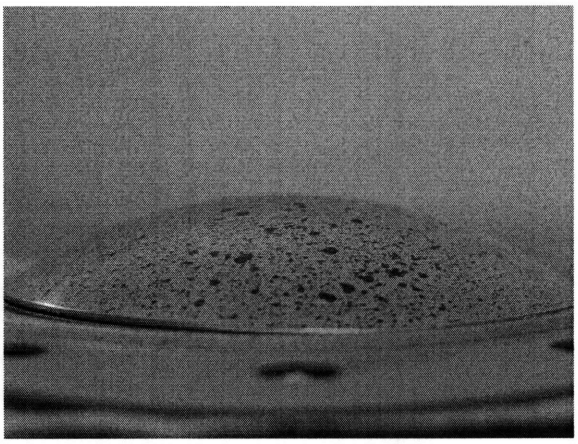

(b) Profile view of the bulge

(c) Fracture at the clamped edge

Figure 21: Results of first experiment (without fillet)

The point of fracture developed at the clamped edge of the bulge. The fracture occurred with a loud crack and the hydraulic oil flowed out from the crack but was contained within the upper flange. No jet or large spray was observed. This test was intended to investigate the importance of the fillet at the clamped edge as well as to determine the extent of spray upon fracture, such that the optical measuring system can be employed effectively.

Firstly, without a fillet on the inner diameter of the circular die, high stress was localized at the hard corner. As expected, fracture resulted at the edge instead of at the center of the bulge. Therefore, it is important to introduce the fillet and use Eq. (18) for the calculation of the radius of curvature. However, the size of the fillet cannot be easily determined as it depends on the ductility and thickness of the test material, which would bulge at different degrees.

Secondly, since no jet or large spray was observed, it might be possible to remove the top plastic sheet to eliminate refraction, thereby improving the accuracy of the optical measuring system. Having more accurate measurements, the surface strain and displacement at the top of the dome can then be accurately calculated using the software Vic-3D.

In the second experiment, a fillet of 3mm was introduced on the inner diameter of the same circular die as shown in Figure 22(b). This corrective action removed the hard corner, preventing possible premature failure along the clamped edge as seen in the first experiment. The pictures of the specimen are shown in Figure 23.

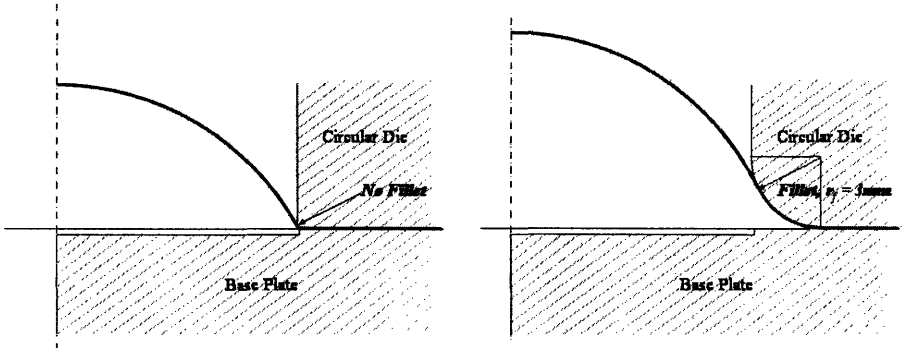

(a) Without fillet (b) With 3mm fillet

Figure 22: Fillet sizes in first and second experiments

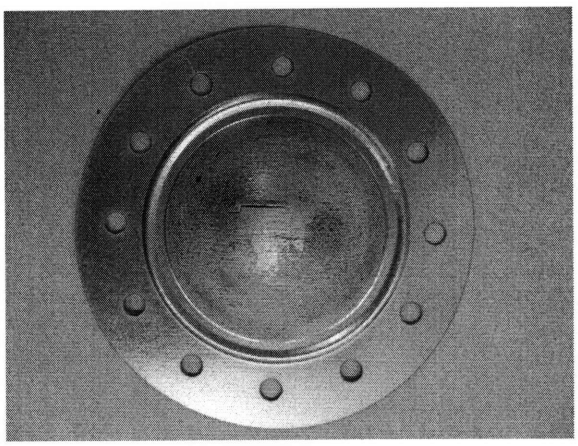

(a) Plan view of the bulge

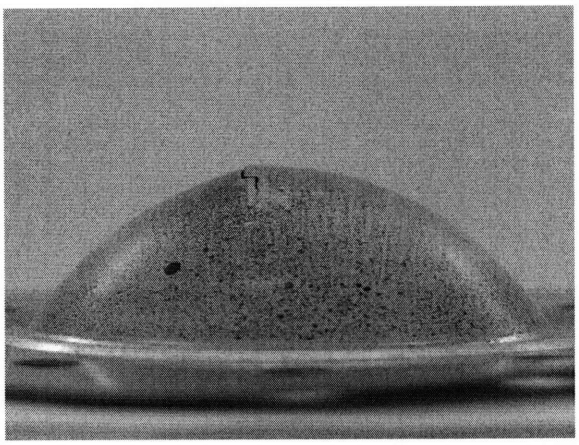

(b) Profile view of the bulge

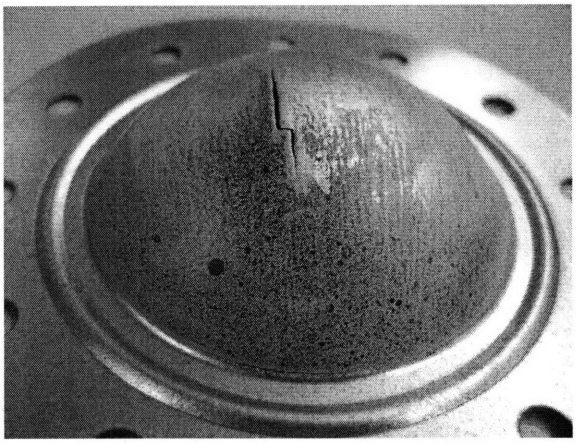

(c) Fracture near the top of the dome

Figure 23: Results of second experiment (with 3mm fillet)

The point of fracture developed near the top of the dome along the rolling direction of the sheet metal. There was no observable high stress area near the circumference of the bulge. The fracture occurred with a loud crack and the hydraulic oil sprayed out from the crack but was contained within the enclosure.

The second experiment validated that the introduction of a fillet on the inner diameter of the circular die helped relieve the high stresses at the clamped edge, thus allowing the equi-biaxial stress state at the top of the dome to dominate. This was shown by the crack initiation near the top of the dome at a higher pressure of 16.2 MPa in comparison with 12.2 MPa in the first experiment. Theoretically, the highest stress state should occur exactly at the top of the dome. However, crack initiation is a complex phenomenon which could arise due to material imperfection. This requires a further understanding of the material microstructure, and will not be discussed with in this analysis.

The large spray observed in the second experiment poses a problem with the implementation of the optical measuring system. Since an enclosure is required to contain the spray, the optical measuring system would not yield good results due to refraction in the plastic sheet. The optical measuring system may therefore not be suitable for this application. Since a closed-form solution has been derived in Section 4.1, it is possible to perform post-experiment measurements to determine the sheet thickness h, at the top of the dome, and the radius of curvature R, by measuring the shape of the dome. However, this only gives one point on the stress-strain curve at the point of fracture. Alternatively, an extensometer could be introduced to measure the dome height throughout the experiment. Using Eq. (18) and (19), the R and h can be estimated geometrically, thus generating the entire stress-strain relationship for the equi-biaxial stress state.

Chapter 5

Conclusions

5.1 Summary of results

The hydraulic bulge test apparatus was designed, built and successfully tested on a generic sheet metal to create an equi-biaxial stress state for the study of material properties. The challenge of the large spray during fracture rendered the optical measuring system less favourable for this type of experiment. The alternative method is to introduce an extensometer to measure the dome height and make use of geometrical relationships to determine the equi-biaxial stress state during the bulging process. Two methods were discussed in the theoretical analysis of the experiment. One method is by the direct measurement of the specimen after the experiment; the other method is using geometrical relationships under the assumption that the dome is spherical in shape. The FEM software, Abaqus, was also introduced as a simulation tool for the prediction of the stress-strain relationship of the material in equi-biaxial tension. Besides the construction of the hydraulic bulge test apparatus, a set of experimental procedures were also introduced as a reference guide for future users of this equipment. This report also stepped through the different phases of design, from determining requirements to design parameters and final product development, highlighting the various challenges in the process.

5.2 Future work

The current equipment has been confirmed to effectively perform a hydraulic bulge test, but has limited measuring capabilities as the optical measuring system could not be used

effectively in this case. Therefore, another method of data collection and analysis has been proposed in Chapter 4, which could overcome the existing shortcoming. There are also many other work to be carried out using this piece of equipment. The following list presents the future work required to meet the grand objective for the categorization of AHSS in the ICL:

- Introduction of an extensometer for acquiring dome height data
- Comparison of DP450 experimental results with numerical simulation (in Chapter 4)
- Design of elliptical-shaped die for region around equi-biaxial tension (with reference to Rees (1994))
- Comparison of results with Nakazima punch test (to calibrate the effect of friction)
- Calibration of Bai and Wierzbicki model
- Completion of the entire FFLD

Bibliography

Mohr, D., Oswald, M. (2007). A new experimental technique for the multi-axial testing of advanced high strength steel sheets. *Experimental Mechanics*, in press.

Bai, Y., Wierzbicki, T. (2007). A new model of metal plasticity and fracture with pressure and lode dependence. *International Journal of Plasticity*, accepted.

Wierzbicki, T., Bao, Y., Lee, Y.W., Bai, Y. (2005). Calibration and evaluation of seven fracture models. *International Journal of Mechanical Sciences* 47, 719-743.

Spitzig, W.A., Richmond, O. (1984). The effect of pressure on the flow stress of metals. *Acta Metallurgica*, 32(3), 457-463.

Wilson, C.D. (2002). A critical reexamination of classical metal plasticity. *Journal of Applied Mechanics*, Transactions of ASME, 69(1), 63-68.

Barsoum, I., Faleskog, J. (2006). Rupture mechanisms in combined tension and shear - Experiments. *International Journal of Solid and Structure*, 44(6), 1768-1786.

Erichsen, A.M. (1914). A new test for thin sheets (in German). *Stahl und Eisen* 34, 879-882.

Olsen, T.Y. (1920). Machines for ductility testing. *Proc Amer Soc Mater* 20, 398-403.

Hecker, S.S. (1974). A cup test for assessing stretchability. *Met Eng* Quart 2, 30-36.

Sachs, G. (1930). A new testing device for deep-drawing (in German). *Metallwirtschaft* 9, 213-218.

Blume, I. (1922). Assessment of the deep-drawability of sheets (in German). *Metallbörse* 12, 1945-1946.

Chung, S.Y., Swift, H.W. (1951). Cup-drawing from a flat blank. *Proc Inst Mech Eng*, 199-223.

Swift, H.W. (1954). The mechanism of a simple deep-drawing operation. *Sheet Metal Ind* 31, 817-828.

Fukui, S. (1939). Researches on the deep-drawing process. *Scientific Papers of the I.P.C.R.* 34, 1422-1527.

ASTM E 290-97a: Standard test method for bend testing of material for ductility.

Demeri, M.Y. (1981). The stretch-bend forming of sheet metal. *J Appl Metalwork* 2, 3-10.

Brozzo, P., De Luca, B., Rendina, R. (1972). A new method for the prediction of the formability limits of metal sheets. *7th Biennual Congr of the IDDRG*, Amsterdam.

Keeler, S.P. (1961). Plastic instability and fracture in sheet stretched over rigid punches. *Thesis, Massachusetts Institute of Technology*, Boston, MA.

Marciniak, Z. (1971). Limits of sheet metal formability (in Polish). Warsaw, WNT

Nakazima, K., Kikuma, T., Hasuka, K. (1971). Study on the formability of steel sheets. *Yawata Tech Rep* No. 284, 678-680.

Hasek, V. (1973). On the strain and stress states in drawing of large unregular sheet metal components (in German). *Berichte aus dem Institute für Umformtechnik*, Universität Stuttfart, Nr. 25, Essen, Girardet.

Ranta-Eskola, A.J. (1979). Use of the hydraulic bulge test in biaxial tensile testing. *Int. J. Mech. Sci.* 21, 457-465.

IIST (2005). Advanced high strength steel (AHSS) application guidelines. *International Iron and Steel Institute*, March 2005.

Ugural, A.C., Fenster, S.K. (1995). Advanced strength and applied elasticity. 4th edition, Prentice Hall.

Gutscher, G., Wu, H.C., Ngaile, G., Altan, T. (2004). Determination of flow stress for sheet metal forming using the viscous pressure bulge (VPB) test. *Journal of Materials Processing Technology* 146, 1-7.

Panknin, W. (1959). The hydraulic bulge test and the determination of the flow stress curves. *Dissertation, Institute for Metal Forming Technology*, University of Stuttgart, Germany.

Gologranc, F. (1975). Evaluation of the flow stress curve with the continuous hydraulic bulge test. *Dissertation, Institute for Metal Forming Technology*, University of Stuttgart, Germany.

Chakrabarty, J., Alexander, J.M. (1970). Hydrostatic bulging of circular diaphragms. *Phil Mag* 7, 1133-1142.

Bressen, J.D., Williams, J.A. (1982). The use of a shear instability criterion to predict local necking in sheet metal deformation. *Int J. Mech Sci* 25, 155-168.

Rees, D.W.A. (1994). Plastic flow in the elliptical bulge test. *Int J. Mech Sci* 37, 373-389.

Hill, R. (1950). A theory of the plastic bulging of a metal diaphragm by lateral pressure. *Phil Mag* 41, 1133.

Ross, E.W., Prager, W. (1954). On the theory of the bulge test. *Q. Appl Math* 12, 86.

Appendix A

Detailed Design of the Hydraulic Bulge Test Apparatus

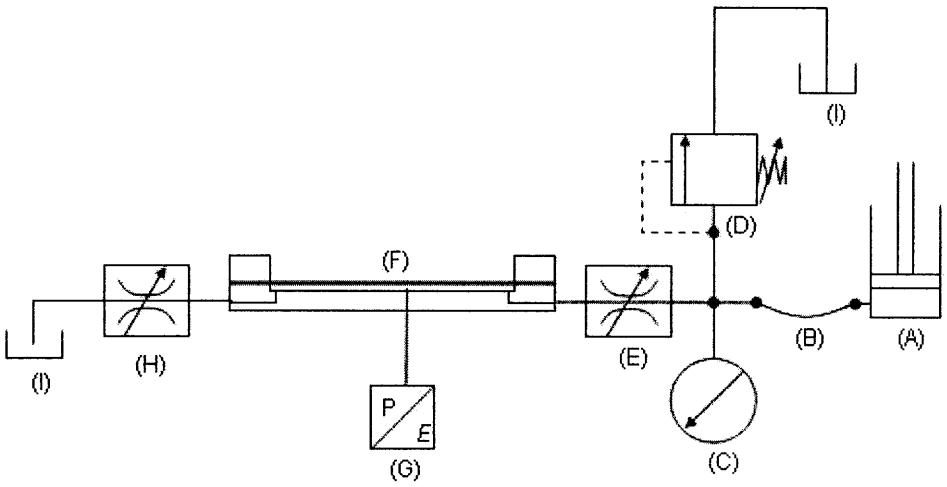

	Component	Model	Qty
A1	Hydraulic Cylinder	RC-108	1
A2	Quick Coupler	CR-400	1
A3	Base Plate	JBI-10	1
A4	Male Stud (coupling for MTS)	Custom Made	1
B1	Flexible Hose	H-9203	1
B2	Cross Fitting	FZ-1613	1
C1	Pressure Gauge	G-2535	1
C2	Bushing	FZ-1630	1
D1	Pressure Relief Valve w Return Line	V-152	1
D2	Hex Nipple	FZ-1617	1
E1	Needle Valve, Inlet	V-82	1
E2	Quick Coupler	McMaster Part# 53455K55 Part# 53455K28	1
E3	Hex Nipple	FZ-1617	1
E4	Bushing	FZ-1630	1
E5	Hex Nipple	FZ-1608	1
F1	Test Chamber	Custom Made	1
F2	Chamber Stand	Custom Made	1
G	Pressure Transducer	PDCR 4000	1
H1	Needle Valve, Outlet	V-82	1
H2	Bushing	FZ-1630	1
H3	Hex Nipple	FZ-1608	1
I	Hydraulic Tank w Hydraulic Oil	HF-101	1

All components (under pressure) rated up to 10,000psi

APPENDIX A. DETAILED DESIGN OF THE HYDRAULIC BULGE TEST APPARATUS

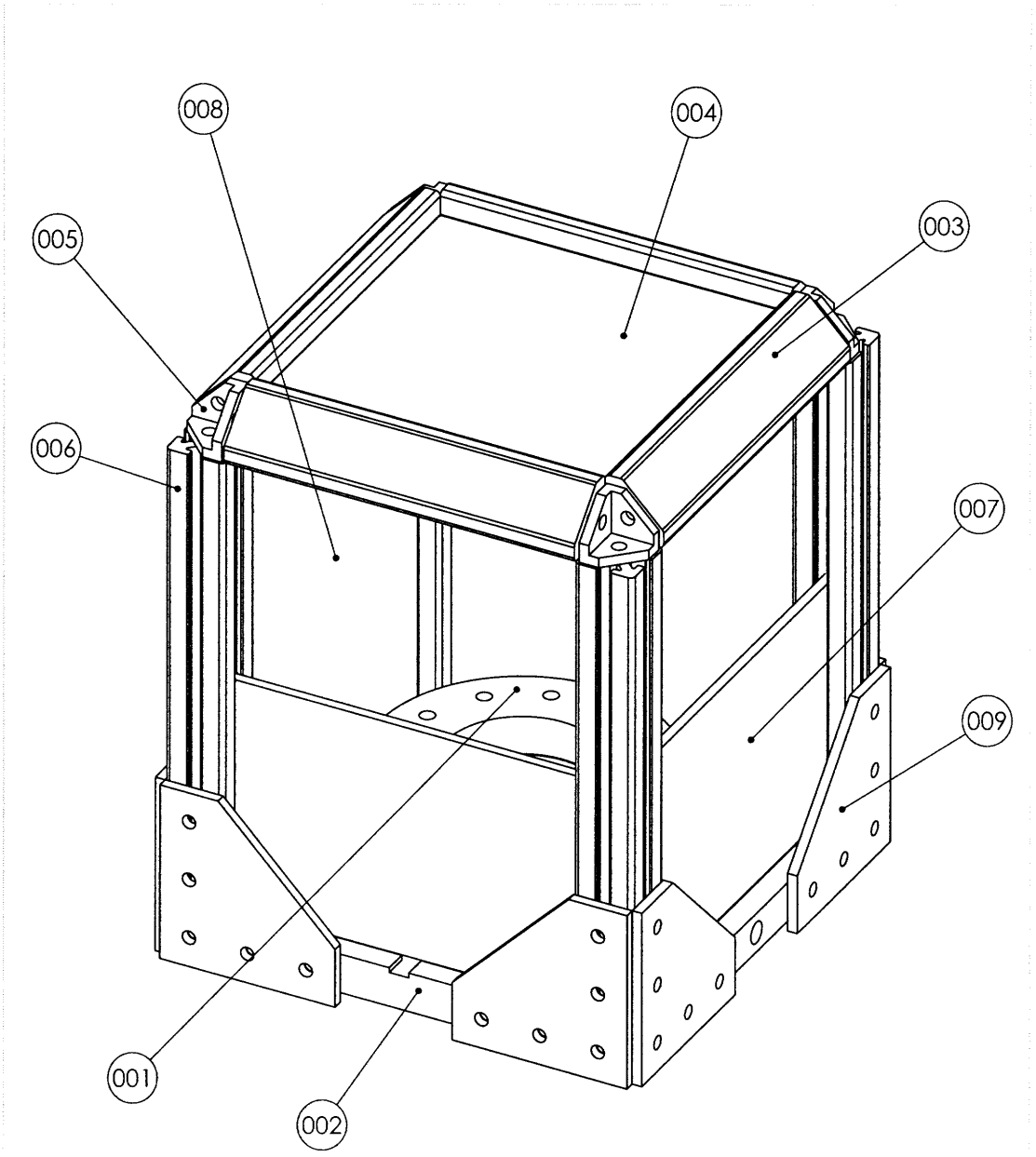

PROPRIETARY AND CONFIDENTIAL THE INFORMATION CONTAINED IN THIS DRAWING IS THE SOLE PROPERTY OF <INSERT COMPANY NAME HERE>. ANY REPRODUCTION IN PART OR AS A WHOLE WITHOUT THE WRITTEN PERMISSION OF <INSERT COMPANY NAME HERE> IS PROHIBITED.	DIMENSIONS ARE IN INCHES TOLERANCES: FRACTIONAL ± ANGULAR: MACH ± BEND ± TWO PLACE DECIMAL ± THREE PLACE DECIMAL ± MATERIAL FINISH		NAME	DATE	CHAMBER
		DRAWN	C W KOH	7/24/07	
		CHECKED			
		ENG APPR.			
		MFG APPR.			
		Q.A.			
		COMMENTS:			
NEXT ASSY USED ON APPLICATION	DO NOT SCALE DRAWING				SIZE A DWG. NO. HBTA-000 REV. 0 SCALE:1:1 WEIGHT: SHEET 1 OF 1

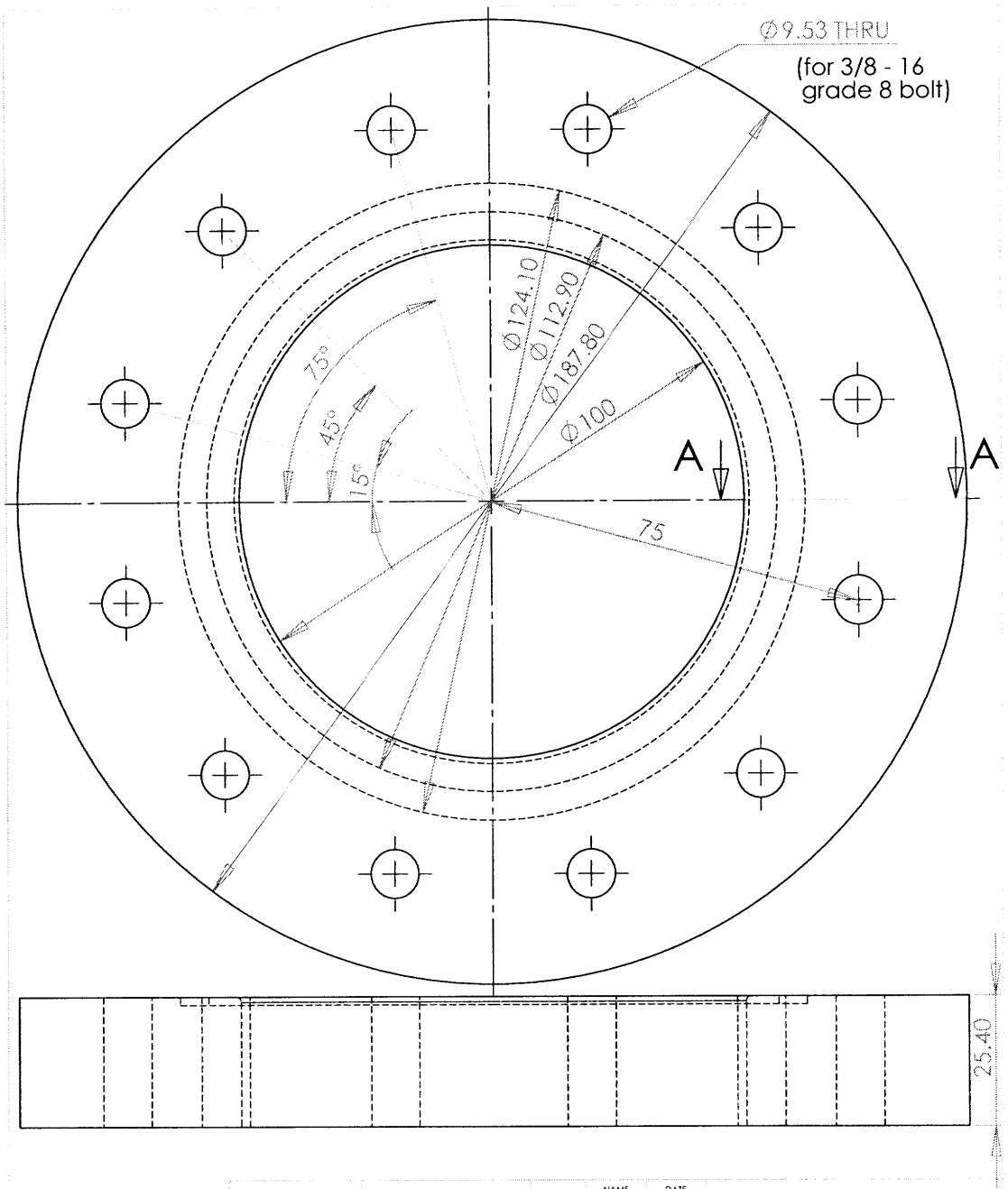

DIMENSIONS ARE IN INCHES		NAME / DATE
TOLERANCES:	DRAWN	C W KOH 12/4/07
FRACTIONAL ±	CHECKED	
ANGULAR: MACH ± BEND ±	ENG APPR.	
TWO PLACE DECIMAL ±	MFG APPR.	
THREE PLACE DECIMAL ±	Q.A.	
MATERIAL	COMMENTS:	
FINISH		
NEXT ASSY USED ON		
APPLICATION	DO NOT SCALE DRAWING	

TITLE: UPPER FLANGE (SHEET 1)

SIZE A DWG. NO. HBTA - 001-01 REV 1

SCALE:1:1 WEIGHT: SHEET 1 OF 2

APPENDIX A. DETAILED DESIGN OF THE HYDRAULIC BULGE TEST APPARATUS

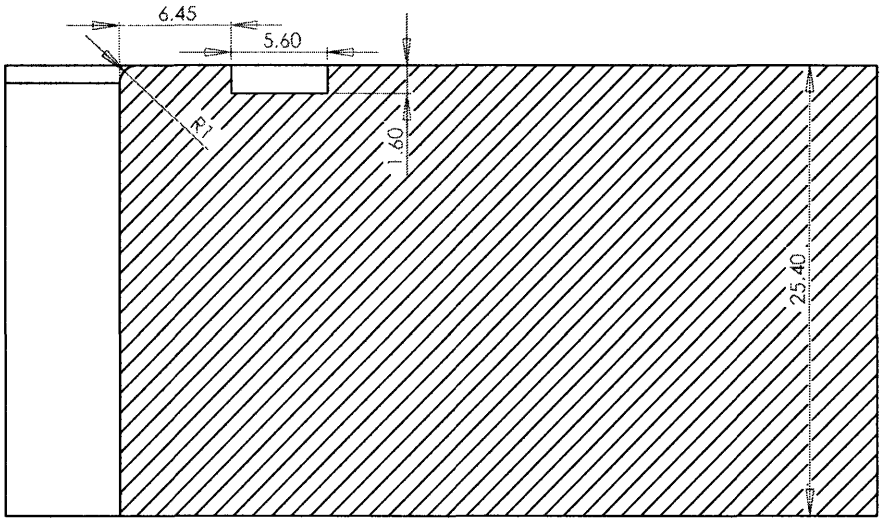

SECTION A-A
SCALE 4 : 1

UNLESS OTHERWISE SPECIFIED:
DIMENSIONS ARE IN INCHES
TOLERANCES:
FRACTIONAL ±
ANGULAR: MACH ± BEND ±
TWO PLACE DECIMAL ±
THREE PLACE DECIMAL ±
INTERPRET GEOMETRIC TOLERANCING PER:
MATERIAL
FINISH
DO NOT SCALE DRAWING

	NAME	DATE
DRAWN	C W KOH	12/4/07
CHECKED		
ENG APPR.		
MFG APPR.		
Q.A.		
COMMENTS:		

TITLE:
UPPER FLANGE
(SHEET 2)

SIZE	DWG. NO.	REV
A	HBTA-001-02	1

SCALE: 1:1 WEIGHT: SHEET 2 OF 2

NEXT ASSY USED ON
APPLICATION

5 4 3 2 1

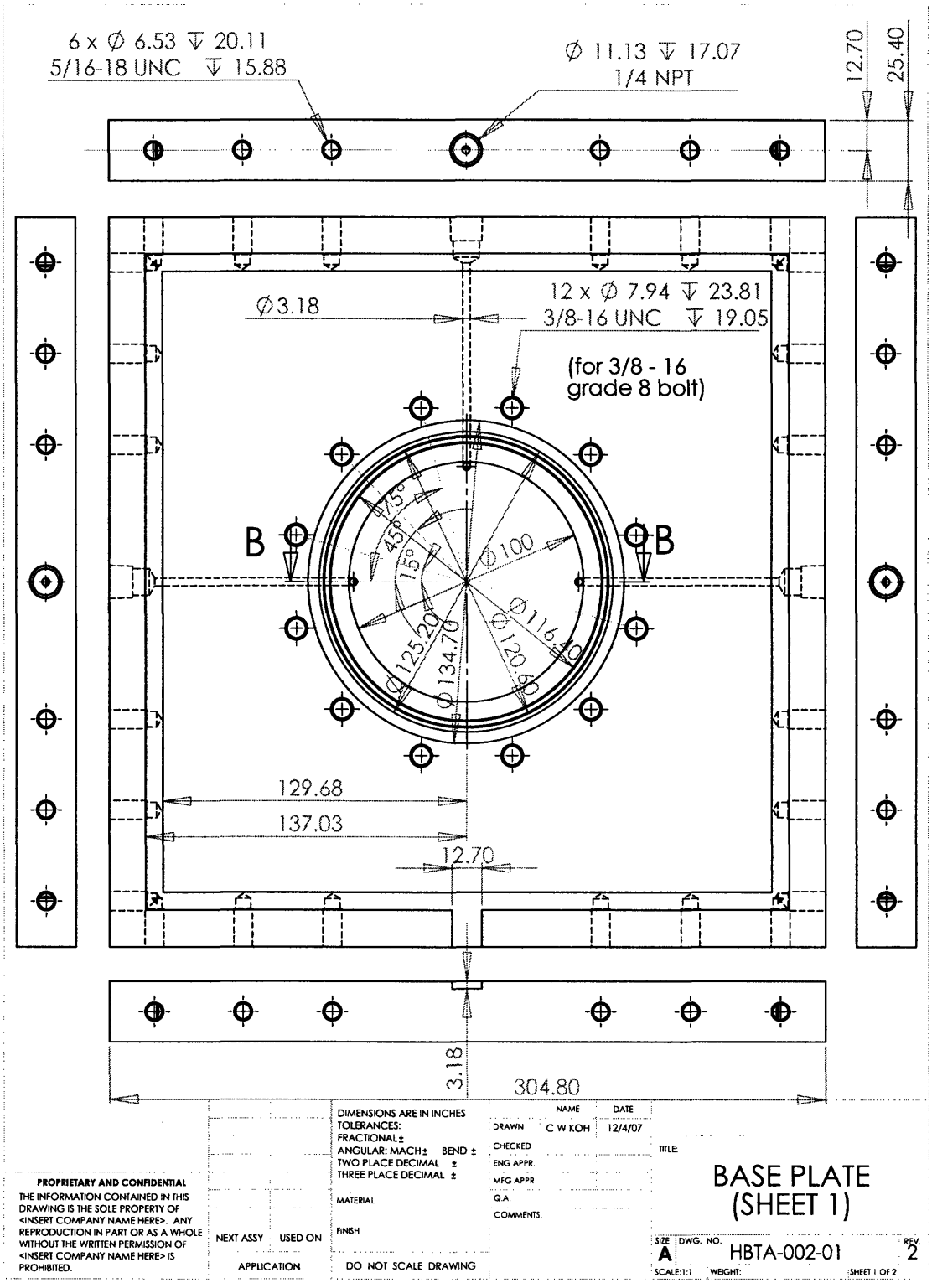
6 x Ø 6.53 ↧ 20.11
5/16-18 UNC ↧ 15.88
Ø 11.13 ↧ 17.07
1/4 NPT
12.70
25.40
Ø3.18
12 x Ø 7.94 ↧ 23.81
3/8-16 UNC ↧ 19.05
(for 3/8 - 16
grade 8 bolt)
B
B
75°
45°
15°
Ø100
Ø116.40
Ø120.65
Ø125.20
Ø134.70
129.68
137.03
12.70
3.18
304.80
PROPRIETARY AND CONFIDENTIAL
THE INFORMATION CONTAINED IN THIS DRAWING IS THE SOLE PROPERTY OF <INSERT COMPANY NAME HERE>. ANY REPRODUCTION IN PART OR AS A WHOLE WITHOUT THE WRITTEN PERMISSION OF <INSERT COMPANY NAME HERE> IS PROHIBITED.
NEXT ASSY
USED ON
APPLICATION
DIMENSIONS ARE IN INCHES
TOLERANCES:
FRACTIONAL ±
ANGULAR: MACH ± BEND ±
TWO PLACE DECIMAL ±
THREE PLACE DECIMAL ±
MATERIAL
FINISH
DO NOT SCALE DRAWING
NAME DATE
DRAWN C W KOH 12/4/07
CHECKED
ENG APPR.
MFG APPR
Q.A.
COMMENTS
TITLE:
BASE PLATE
(SHEET 1)
SIZE A
DWG. NO. HBTA-002-01
REV 2
SCALE:1:1
WEIGHT:
SHEET 1 OF 2

APPENDIX A. DETAILED DESIGN OF THE HYDRAULIC BULGE TEST APPARATUS

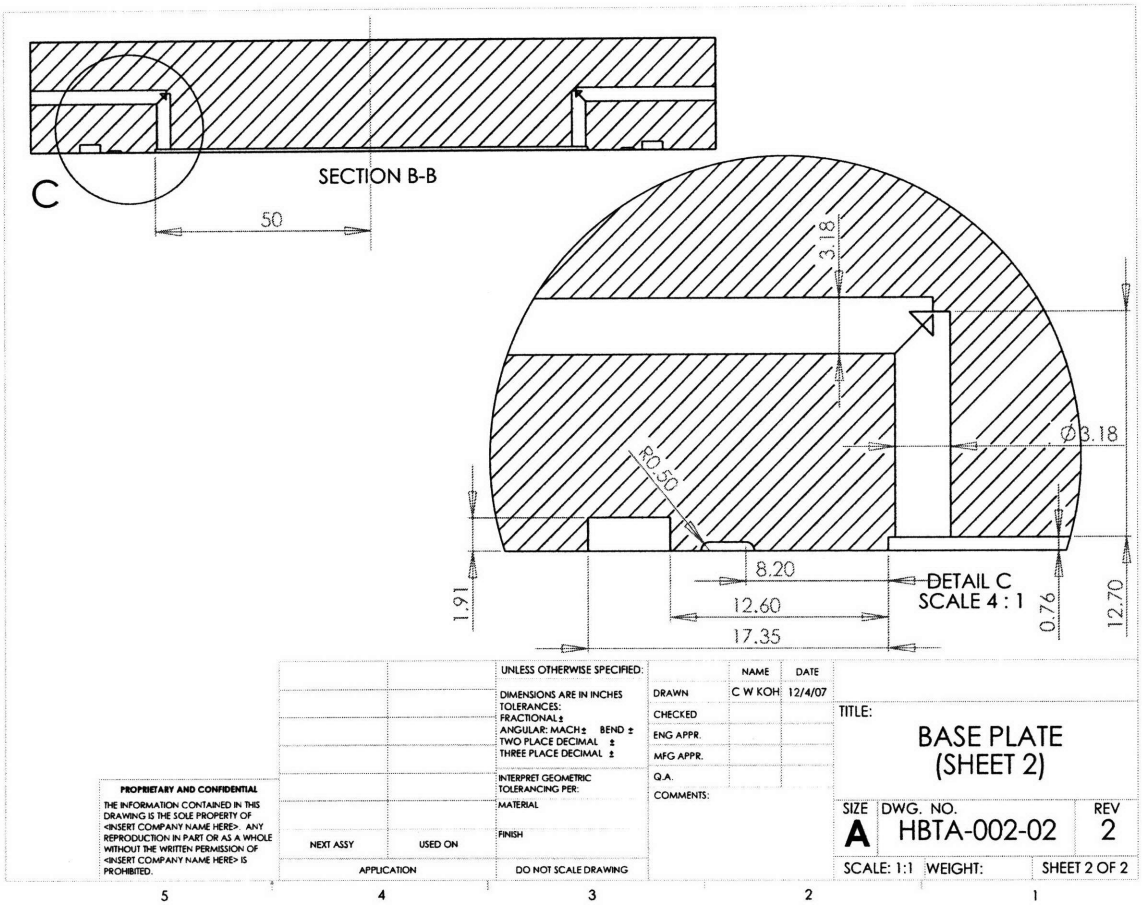

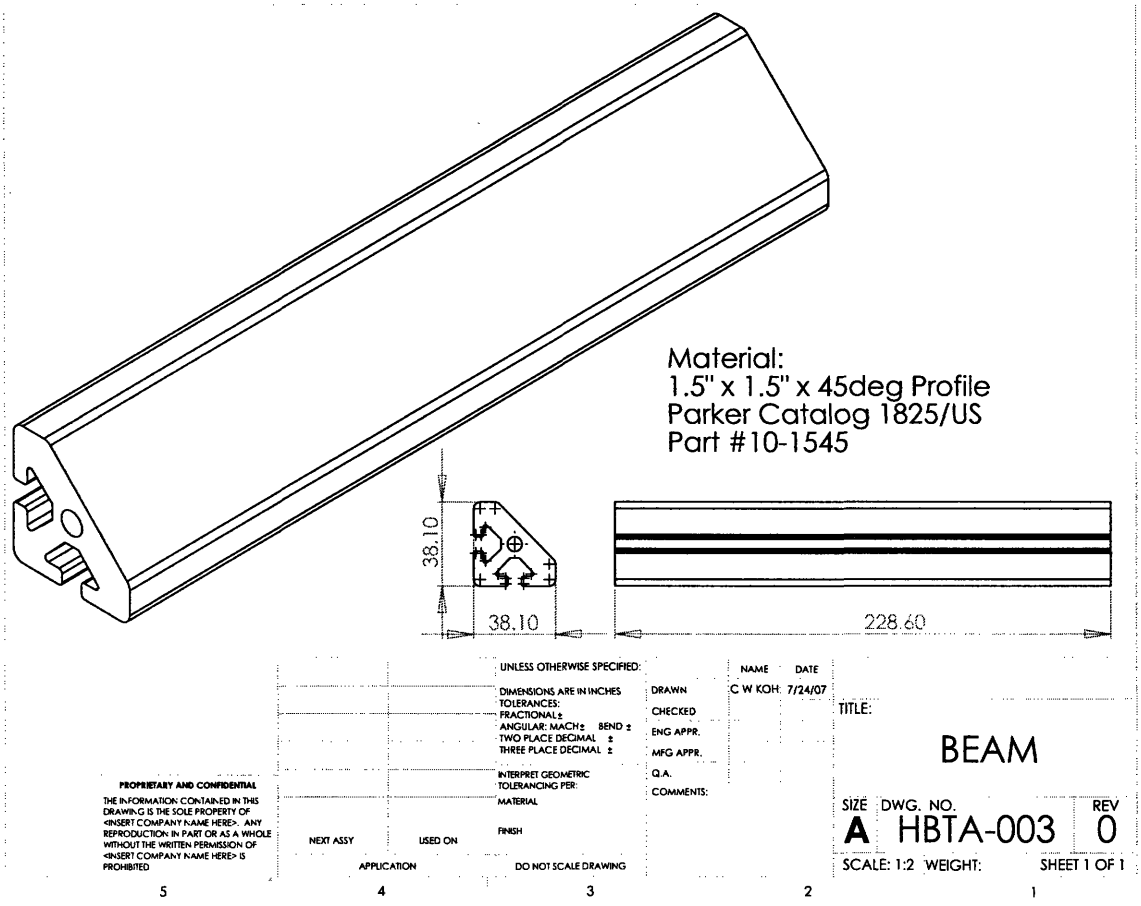
Material:
1.5" x 1.5" x 45deg Profile
Parker Catalog 1825/US
Part #10-1545
38.10
38.10
228.60
UNLESS OTHERWISE SPECIFIED:
DIMENSIONS ARE IN INCHES
TOLERANCES:
FRACTIONAL ±
ANGULAR: MACH ± BEND ±
TWO PLACE DECIMAL ±
THREE PLACE DECIMAL ±
INTERPRET GEOMETRIC TOLERANCING PER:
MATERIAL
FINISH
DO NOT SCALE DRAWING
NAME DATE
DRAWN C W KOH 7/24/07
CHECKED
ENG APPR.
MFG APPR.
Q.A.
COMMENTS:
NEXT ASSY
USED ON
APPLICATION
PROPRIETARY AND CONFIDENTIAL
THE INFORMATION CONTAINED IN THIS DRAWING IS THE SOLE PROPERTY OF <INSERT COMPANY NAME HERE>. ANY REPRODUCTION IN PART OR AS A WHOLE WITHOUT THE WRITTEN PERMISSION OF <INSERT COMPANY NAME HERE> IS PROHIBITED
TITLE:
BEAM
SIZE DWG. NO. REV
A HBTA-003 0
SCALE: 1:2 WEIGHT: SHEET 1 OF 1
5
4
3
2
1

APPENDIX A. DETAILED DESIGN OF THE HYDRAULIC BULGE TEST APPARATUS

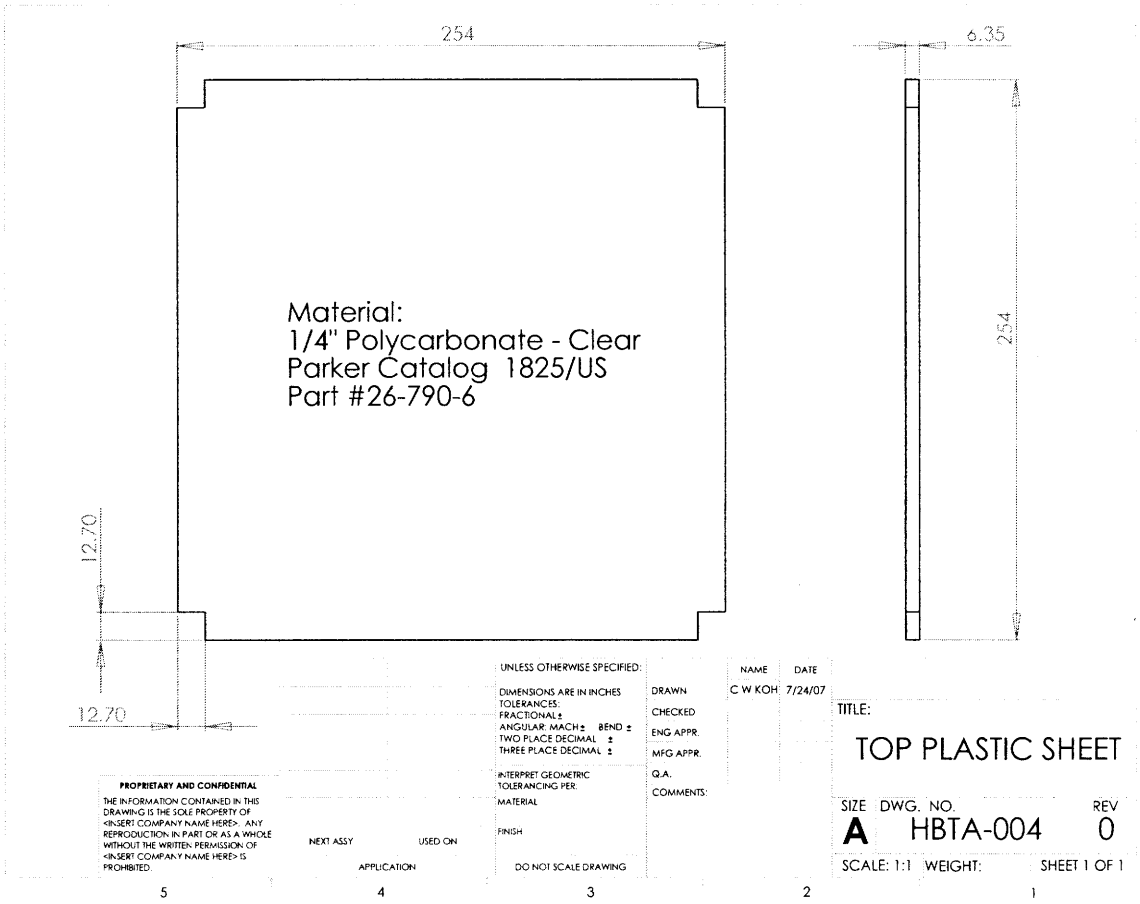

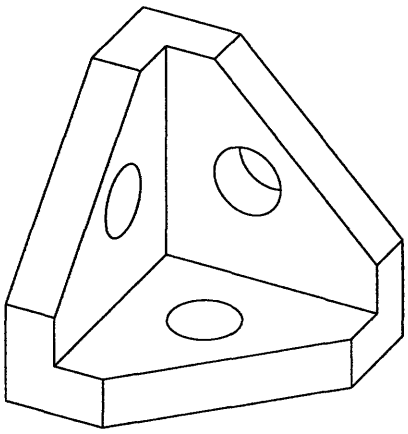

Material:
Corner Bracket 1.5"
Parker Catalog 1825/US
Part #22-153

UNLESS OTHERWISE SPECIFIED:
DIMENSIONS ARE IN INCHES
TOLERANCES:
FRACTIONAL ±
ANGULAR: MACH ± BEND ±
TWO PLACE DECIMAL ±
THREE PLACE DECIMAL ±
INTERPRET GEOMETRIC TOLERANCING PER:
MATERIAL
FINISH
DO NOT SCALE DRAWING

	NAME	DATE
DRAWN	C W KOH	7/24/07
CHECKED		
ENG APPR.		
MFG APPR.		
Q.A.		
COMMENTS:		

TITLE: CORNER BRACKET

SIZE A | DWG. NO. HBTA-005 | REV 0

SCALE: 1:1 WEIGHT: SHEET 1 OF 1

NEXT ASSY USED ON
APPLICATION

5 4 3 2 1

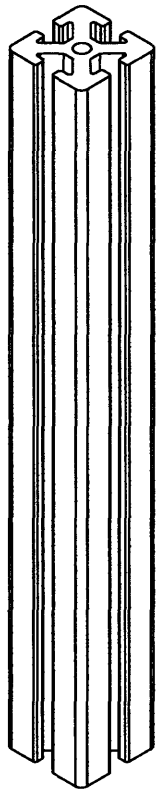

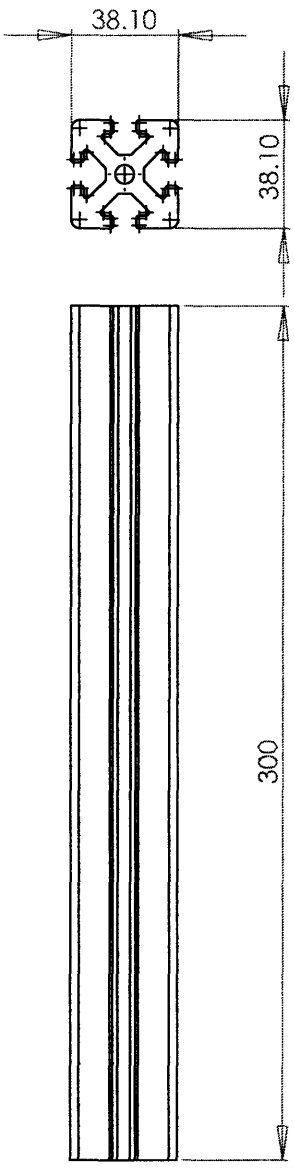

Material:
1.5" x 1.5" Heavy Profile
Parker Catalog 1825/US
Part #11-1515

		DIMENSIONS ARE IN INCHES TOLERANCES: FRACTIONAL ± ANGULAR: MACH ± BEND ± TWO PLACE DECIMAL ± THREE PLACE DECIMAL ±		NAME	DATE
			DRAWN	C W KOH	7/24/07
			CHECKED		
			ENG APPR.		
			MFG APPR.		
		MATERIAL	Q.A.		
			COMMENTS:		
NEXT ASSY	USED ON	FINISH			
APPLICATION		DO NOT SCALE DRAWING			

PROPRIETARY AND CONFIDENTIAL
THE INFORMATION CONTAINED IN THIS DRAWING IS THE SOLE PROPERTY OF <INSERT COMPANY NAME HERE>. ANY REPRODUCTION IN PART OR AS A WHOLE WITHOUT THE WRITTEN PERMISSION OF <INSERT COMPANY NAME HERE> IS PROHIBITED.

PILLAR

SIZE	DWG. NO.	REV.
A	HBTA-006	0
SCALE: 1:1	WEIGHT:	SHEET 1 OF 1

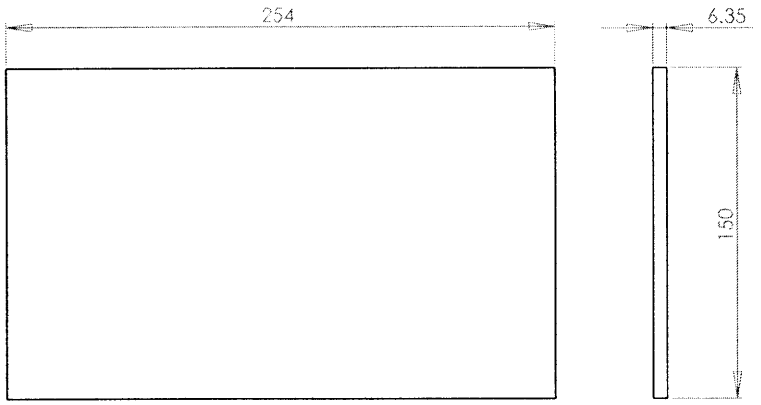

Material:
1/4" Polycarbonate - Clear
Parker Catalog 1825/US
Part #26-790-6

UNLESS OTHERWISE SPECIFIED:
DIMENSIONS ARE IN INCHES
TOLERANCES:
FRACTIONAL ±
ANGULAR: MACH ± BEND ±
TWO PLACE DECIMAL ±
THREE PLACE DECIMAL ±
INTERPRET GEOMETRIC TOLERANCING PER:
MATERIAL
FINISH
NEXT ASSY | USED ON
APPLICATION
DO NOT SCALE DRAWING

DRAWN
CHECKED
ENG APPR.
MFG APPR.
Q.A
COMMENTS:

NAME DATE
C W KOH 7/24/07

TITLE:
PLASTIC SHEET

SIZE A | DWG. NO. HBTA-007 | REV 0
SCALE: 1:1 WEIGHT: SHEET 1 OF 1

5 4 3 2 1

APPENDIX A. DETAILED DESIGN OF THE HYDRAULIC BULGE TEST APPARATUS

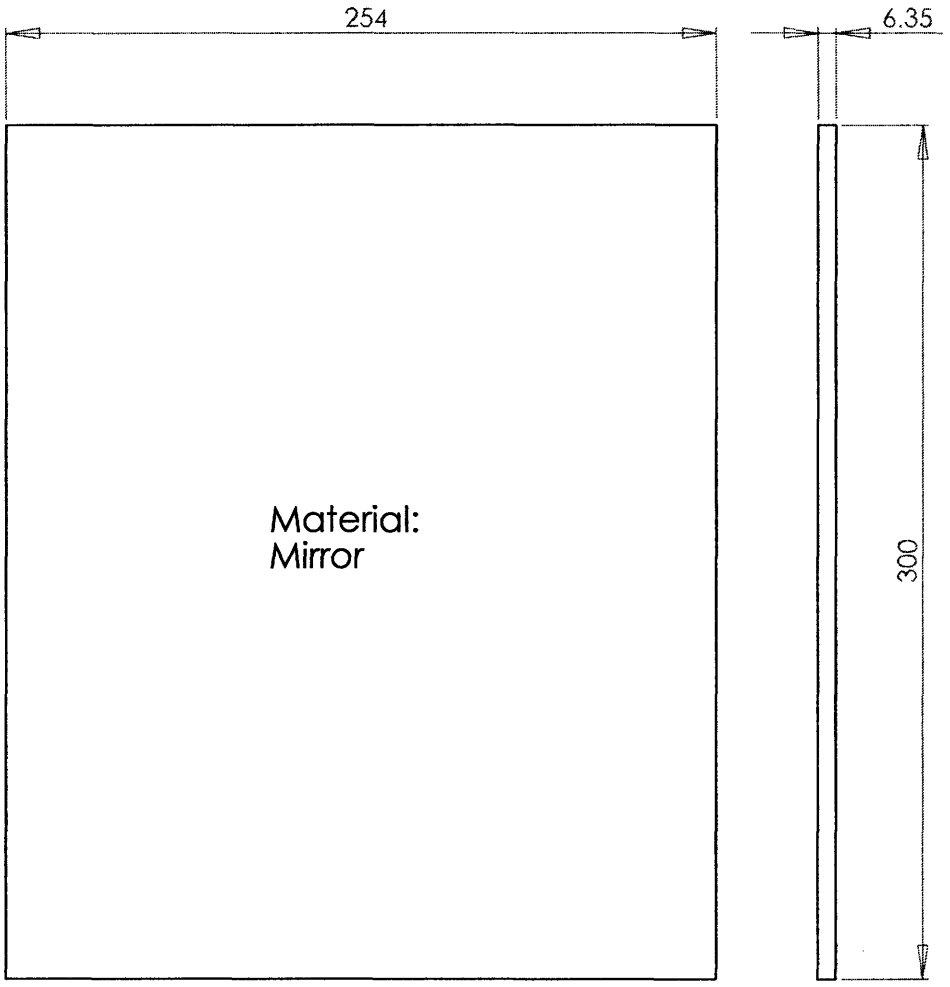

		DIMENSIONS ARE IN INCHES		NAME	DATE
		TOLERANCES:	DRAWN	C W KOH	7/24/07
		FRACTIONAL ±	CHECKED		
		ANGULAR: MACH ± BEND ±	ENG APPR.		
		TWO PLACE DECIMAL ±	MFG APPR.		
		THREE PLACE DECIMAL ±	Q.A.		
		MATERIAL	COMMENTS:		
NEXT ASSY	USED ON	FINISH			
APPLICATION		DO NOT SCALE DRAWING			

PROPRIETARY AND CONFIDENTIAL

THE INFORMATION CONTAINED IN THIS DRAWING IS THE SOLE PROPERTY OF <INSERT COMPANY NAME HERE>. ANY REPRODUCTION IN PART OR AS A WHOLE WITHOUT THE WRITTEN PERMISSION OF <INSERT COMPANY NAME HERE> IS PROHIBITED.

MIRROR SHEET

SIZE A | DWG. NO. HBTA-008 | REV. 0

SCALE: 1:1 | WEIGHT: | SHEET 1 OF 1

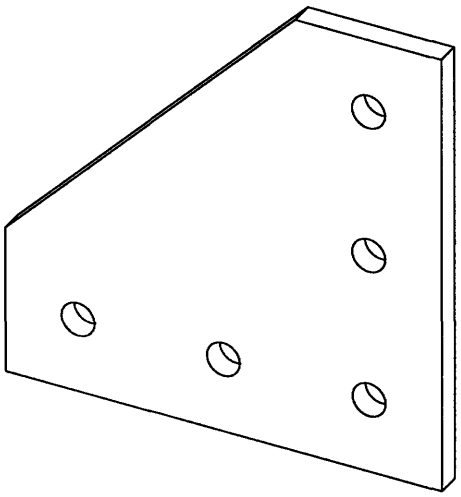

Material:
Joining Plate, Corner 4.5" x 4.5"
Parker Catalog 1825/US
Part #20-304

PROPRIETARY AND CONFIDENTIAL THE INFORMATION CONTAINED IN THIS DRAWING IS THE SOLE PROPERTY OF <INSERT COMPANY NAME HERE>. ANY REPRODUCTION IN PART OR AS A WHOLE WITHOUT THE WRITTEN PERMISSION OF <INSERT COMPANY NAME HERE> IS PROHIBITED.	NEXT ASSY / USED ON APPLICATION	UNLESS OTHERWISE SPECIFIED: DIMENSIONS ARE IN INCHES TOLERANCES: FRACTIONAL ± ANGULAR: MACH ± BEND ± TWO PLACE DECIMAL ± THREE PLACE DECIMAL ± INTERPRET GEOMETRIC TOLERANCING PER: MATERIAL FINISH DO NOT SCALE DRAWING	NAME / DATE DRAWN C W KOH 7/24/07 CHECKED ENG APPR. MFG APPR. Q.A. COMMENTS:	TITLE: CORNER SIZE DWG. NO. REV A HBTA-009 0 SCALE: 1:2 WEIGHT: SHEET 1 OF 1	
5	4	3	2	1	

Parts List			
S/No	**Component Description**	**Model / Part Number**	**Qty**
A	**Hydraulics**		
1	Hydraulic cylinder, 10,000 psi rated, 18 cu. in. capacity, 10 stroke	Enerpac RC-108	1
2	Quick Coupler	Enerpac CR-400	1
3	Base plate for 10 ton cylinder	Enerpac JBI-10	1
4	Flexible hose, 10,000 psi	Enerpac HC-9203	1
5	Pressure gauge, $2^1/_2$" diameter with 1/4" NPT ports, bottom mount	Enerpac G2535L	1
6	Pressure relief valve, 10,000 psi, 3/8" NPT female ports	Enerpac V-152	1
7	Needle Valve, 10,000 psi, 3/8" NPTF female ports	Enerpac V-82	2
8	Cross fitting, 10,000 psi, 3/8" NPT female ports	Enerpac FZ-1613	1
9	Bushing, 3/8×1/4" female, 10,000 psi	Enerpac FZ-1630	3
10	Hex nipple with 3/8" NPT female ports	Enerpac FZ-1617	2
11	Hex nipple with 3/8" NPT female ports	Enerpac FZ-1608	2
12	Hydraulic tank, 1 gallon with oil	Enerpac HF-101	1
13	Pressure transducer, 3100 series, 0-10,000 psi high pressure, 0-10V output	Gems 3100S10KPS02E	1
14	Pressure transducer cable, M12 cord set	Gems 557703-03M0	1
15	Quick Coupler	McMaster Part Nos. #53455K55, #53455K28	1

continued on next page

Parts List			
S/No	**Component Description**	**Model / Part Number**	**Qty**
B	**Test Chamber**		
1	Upper flange	Mass Bay Engg - refer to drawing HBTA001-R1	1
2	Base plate	Mass Bay Engg - refer to drawing HBTA002-R2	1
3	Draw bead, grip ring, 1/8" diameter, T316 spring steel from Malin Co.	Mass Bay Engg	1
4	Bolt, grade 8	Mass Bay Engg	12
5	Washer	Mass Bay Engg	12
6	O-ring	Mass Bay Engg	1
C	**Enclosure**		
1	Beam, length 228.6mm	Parker IPS # 10-1545 - refer to drawing HBTA003-R0	4
2	Top plastic sheet, clear polycarbonate top panel with four notches	Parker IPS # 26-790-6 - refer to drawing HBTA004-R0	1
3	Corner bracket, 1.5"	Parker IPS #22-153 - refer to drawing HBTA005-R0	4
4	Pillar, length 300mm	Parker IPS #11-1515 - refer to drawing HBTA006-R0	4
5	Plastic sheet, clear polycarbonate lower panel	Parker IPS #26-790-6 - refer to drawing HBTA007-R0	2
6	Mirror sheet, mirrored acrylic panel	Hart Supply - refer to drawing HBTA008-R0	2
7	Corner, joining plate	Parker IPS #20-304 - refer to drawing HBTA009-R0	8
8	Gasket, for sheet edges	Cocus Solutions	
9	Screw, $5/16 - 18 \times 5/8$"	Parker IPS #25-110-5	40
10	T-nut, $5/16 - 18$	Parker IPS #25-046	8

continued on next page

Parts List			
S/No	**Component Description**	**Model / Part Number**	**Qty**
D	**Miscellaneous**		
1	Thread sealant for hydraulics, Loctite PTFE/Anaerobic pipe thread sealant for metal threads, #545, 1.69oz (50ml) bottle	McMaster Part No. #45855K63	1

Appendix B

Experiment Procedures

Specimen preparation

1. Draw the specimen design using OMAX Layout software - "Specimen Drawing.dxf".

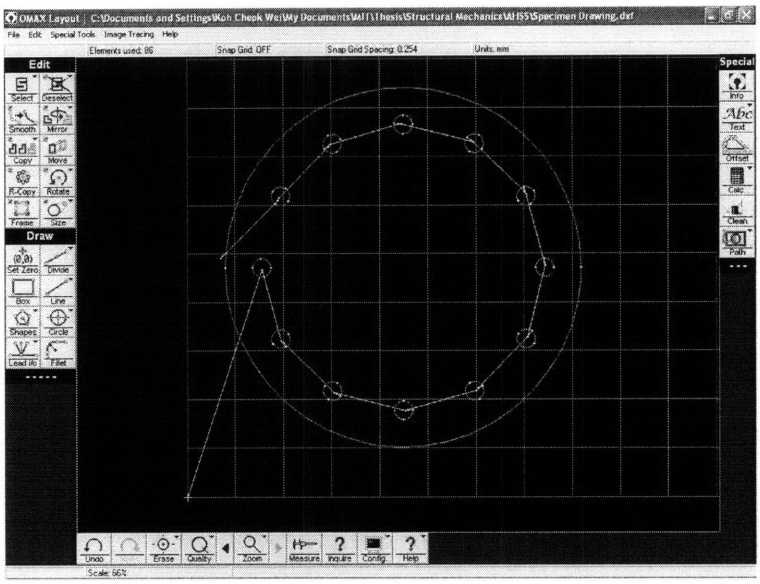

2. Generate the cutting algorithm using OMAX Layout software - "Specimen Drawing.ord".

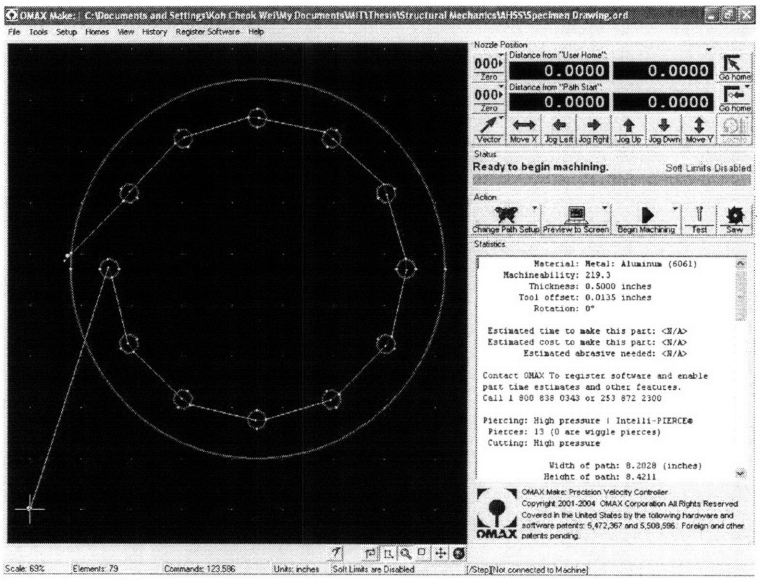

3. Open "Specimen Drawing.ord" at the waterjet cutting terminal to cut the specimen.
4. Clean the specimen thoroughly.

System calibration (Pressure Transducer)

1. Attach the pressure transducer directly to the cylinder plunger.
2. Lower the MTS machine to depress the plunger and record the force in the load cell on the MTS and the voltage output from the pressure transducer at the same time.
3. Calculate the pressure in the cylinder at the corresponding voltage output from the pressure transducer. This calibrates the pressure transducer.

Pre-test preparation

1. Disconnect the Inlet Valve from the Test Chamber to fill the hydraulic system. Take note to lay the cylinder plunger in the horizontal position with the plunger fully extended to minimize air pockets in the system.
2. Shut the Inlet Valve and connect to the Test Chamber.
3. Shut the Outlet Valve and fill the Test Chamber before installing the specimen.
4. Install the specimen by tightening the bolts gradually in a criss-cross manner to evenly spread the load. This may take some effort as the bolts are used to deform the specimen at the draw bead. Use a torque wrench with 30 ft-lb.
5. Open the Outlet Valve and depress the plunger slightly to bleed the system.
6. Shut the Outlet Valve and stop the plunger at the same time when a constant flow is achieved. This ends the preparation of the hydraulic system.

System Calibration (Optical System)

1. Set up the dual camera optical system looking from above the specimen.
2. Place the calibration board at various angles on the specimen to calibrate the space where the bulge is to be formed.
3. Calibrate the optical system using Vic-3D software.

Testing process

1. Use the MTS loading frame to control the displacement of the plunger at 5mm/min.
2. Record the time series data from the MTS load cell, pressure transducer and optical system using the computer until the specimen fractures.
3. Take note of the pressure in the system during the entire experiment by looking at the pressure gauge value in case the pressure becomes extremely high.

Post-test maintenance

1. Drain any spillage from the Test Chamber and wipe the surfaces. Not required to be complete dry as the oil forms a protective layer for the equipment.

Appendix C

Formulae Derivation

C.1 Derivation for the Radius of Curvature, R

Assuming the dome is spherical in shape, the radius of curvature R can then be calculated based on the geometrical relationship between the maximum dome height w_0, blank radius r_0 and fillet radius r_f:

$$R = \frac{(r_0 + r_f)^2 + w_0^2 - 2r_f w_0}{2w_0}$$

The derivation is as follows.

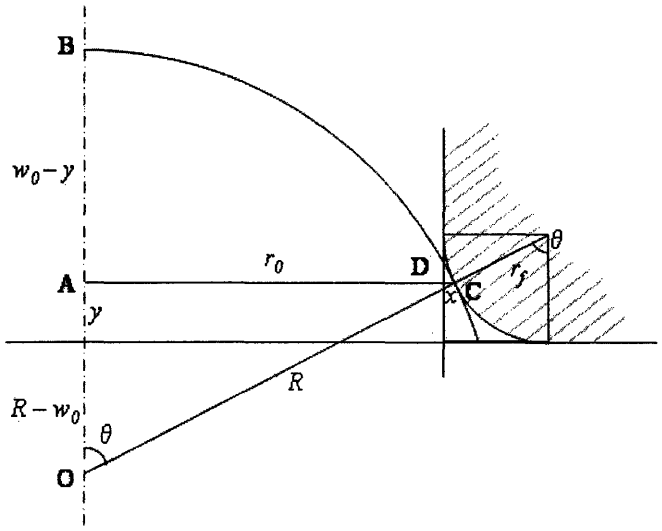

Consider Δ OAC,

$$\sin\theta = \frac{\text{AC}}{\text{OC}} = \frac{r_0 + x}{R} \quad (1)$$

$$\cos\theta = \frac{\text{OA}}{\text{OC}} = \frac{R - w_0 + y}{R} \quad (2)$$

$$x = \text{DC} = r_f(1 - \sin\theta) \quad (3)$$

$$y = r_f(1 - \cos\theta) \quad (4)$$

Combine Eq. (1) and (3)

$$\begin{aligned} \sin\theta &= \frac{r_0 + r_f - r_f\sin\theta}{R} \\ (r_f + R)\sin\theta &= r_0 + r_f \\ \sin\theta &= \frac{r_0 + r_f}{(r_f + R)} \end{aligned} \quad (5)$$

Combine Eq. (2) and (4)

$$\begin{aligned} \cos\theta &= \frac{R - w_0 + r_f - r_f\cos\theta}{R} \\ (r_f + R)\cos\theta &= R + r_f - w_0 \\ \cos\theta &= \frac{r_f + R - w_0}{(r_f + R)} \end{aligned} \tag{6}$$

Using Eq. (5) and (6)

$$\begin{aligned} \sin^2\theta + \cos^2\theta &= 1 \\ \left(\frac{r_0 + r_f}{r_f + R}\right)^2 + \left(\frac{r_f + R - w_0}{r_f + R}\right)^2 &= 1 \\ (r_0 + r_f)^2 + (r_f + R - w_0)^2 &= (r_f + R)^2 \\ (r_0 + r_f)^2 + \cancel{(r_f + R)^2} - 2(r_f + R)w_0 + w_0^2 &= \cancel{(r_f + R)^2} \\ 2w_0(r_f + R) &= (r_0 + r_f)^2 + w_0^2 \\ R &= \frac{(r_0 + r_f)^2 + w_0^2 - 2r_f w_0}{2w_0} \end{aligned}$$

C.2 Derivation for the Sheet Thickness, h, at the Top of the Dome

Besides assuming that the dome is spherical in shape, it is also assumed that the material obeys Tresca's yield criterion and the associated flow rule. Since the sheet metal experiences an equi-biaxial tension at the top of the dome, the flow rule requires the strain rates to satisfy only the incompressibility condition $\dot{\varepsilon} + \dot{\varepsilon}_c + \dot{\varepsilon}_r = 0$ with $\dot{\varepsilon}_c > 0$ and $\dot{\varepsilon}_r > 0$, where $\dot{\varepsilon}$ is the through-thickness strain rate, $\dot{\varepsilon}_c$ is the circumferential strain rate and $\dot{\varepsilon}_r$ is the meridional strain rate.

In addition, using Chakrabarty and Alexander (1970) hypothesis, a strain-hardening dependent parameter $\lambda = 1 - n$ is introduced, where n is the strain-hardening index. Based on these assumptions, and using geometrical relationships, the sheet thickness h at the top of the dome can be estimated by

$$h = h_0 \left[\frac{1}{1 + \left(\frac{w_0}{r_0}\right)^2} \right]^{2-n}$$

where h_0 is the initial sheet thickness, w_0 is the maximum dome height, and r_0 is the blank radius. The derivation of this equation is as follows.

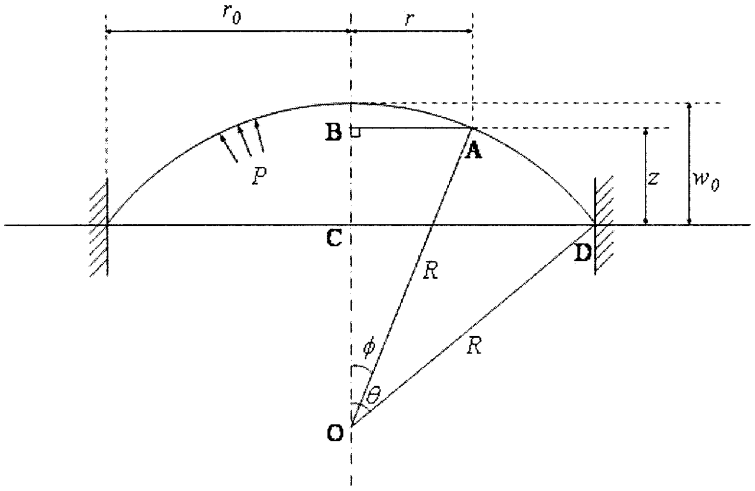

$$r = R \sin \phi \tag{7}$$

Since $\sin\theta = \frac{r_0}{R} \Rightarrow R = \frac{r_0}{\sin\theta}$,

$$\therefore r = r_0 \frac{\sin\phi}{\sin\theta} \tag{8}$$

$$\begin{aligned} w_0 &= R - R\cos\theta \\ &= R(1-\cos\theta) \\ &= \frac{r_0(1-\cos\theta)}{\sin\theta} \\ &= \frac{r_0[1-(1-2\sin^2\frac{\theta}{2})]}{2\sin\frac{\theta}{2}\cos\frac{\theta}{2}} \\ w_0 &= r_0 \tan\frac{\theta}{2} \end{aligned} \tag{9}$$

Using Pythagoras' Theorem for Δ OAB, where Point A is an arbitrary point on the dome surface,

$$\begin{aligned} (R\cos\phi)^2 + r^2 &= R^2 \\ R^2\cos^2\phi + r^2 &= R^2 \\ \cos^2\phi &= \frac{R^2 - r^2}{R^2} \\ \cos\phi &= \sqrt{1 - \frac{r^2}{R^2}} \\ &\approx 1 - \frac{r^2}{2R^2} \qquad \text{(small angle approximation)} \end{aligned}$$

Using Pythagoras' Theorem for Δ OCD,

$$\begin{aligned} r_0^2 + (R - w_0)^2 &= R^2 \\ r_0^2 + R^2 - 2Rw_0 + w_0^2 &= R^2 \\ R &= \frac{r_0^2 + w_0^2}{2w_0} \end{aligned} \tag{10}$$

$$\begin{aligned} \therefore \cos\phi &= 1 - \frac{r^2}{2}\left(\frac{2w_0}{r_0^2 + w_0^2}\right)^2 \\ \cos\phi &= 1 - \frac{2r^2 w_0^2}{(r_0^2 + w_0^2)^2} \end{aligned} \tag{11}$$

Let the radial velocity $v = \dot{r}$, the circumferential strain rate is

$$\dot{\varepsilon}_c = \frac{v}{r} \tag{12}$$

and the meridional strain rate is

$$\dot{\varepsilon}_r = \frac{\partial v}{\partial r} + \dot{\phi}\tan\phi \tag{13}$$

Using material incompressibility condition, $\dot{\varepsilon} + \dot{\varepsilon}_c + \dot{\varepsilon}_r = 0$, where $\dot{\varepsilon}$ is the through-thickness strain rate,

$$\dot{\varepsilon} = -(\dot{\varepsilon}_c + \dot{\varepsilon}_r)$$

The negative sign indicates a through-thickness compression strain rate. From this point forward, the negative sign is dropped.

$$\therefore \dot{\varepsilon} = \dot{\varepsilon}_c + \dot{\varepsilon}_r \tag{14}$$

Combine Eq. (12) and (13),

$$\dot{\varepsilon}_r = \frac{\partial}{\partial r}(r\dot{\varepsilon}_c) + \dot{\phi}\tan\phi \tag{15}$$

Consider rate of change with respect to θ in Eq. (8)

$$\begin{aligned}
\frac{dr}{d\theta} &= r_0\left(\frac{\sin\theta\cos\phi\cdot\frac{d\phi}{d\theta} - \sin\phi\cos\theta}{\sin^2\theta}\right) \\
&= r_0\left(\frac{\dot{\phi}\cos\phi}{\sin\theta} - \frac{\sin\phi\cos\theta}{\sin^2\theta}\right) \\
&= \dot{r} = v
\end{aligned}$$

Substitute into Eq. (12),

$$\begin{aligned}
\dot{\varepsilon}_c &= \frac{v}{r} \\
&= \frac{r_0}{r}\left(\frac{\dot{\phi}\cos\phi}{\sin\theta} - \frac{\sin\phi\cos\theta}{\sin^2\theta}\right) \\
&= \frac{\cancel{r_0}}{\cancel{r_0}\frac{\sin\phi}{\sin\theta}}\left(\frac{\dot{\phi}\cos\phi}{\sin\theta} - \frac{\sin\phi\cos\theta}{\sin^2\theta}\right) \\
\dot{\varepsilon}_c &= \dot{\phi}\cot\phi - \cot\theta
\end{aligned}$$

$$\dot{\phi} = (\dot{\varepsilon}_c + \cot\theta)\tan\phi \tag{16}$$

Substitute Eq. (16) into Eq. (15),

$$\dot{\varepsilon}_r = \frac{\partial}{\partial r}(r\dot{\varepsilon}_c) + (\dot{\varepsilon}_c + \cot\theta)\tan^2\phi$$

From Eq. (8),

$$\begin{aligned} r &= r_0\frac{\sin\phi}{\sin\theta} \\ \frac{\partial r}{\partial\phi} &= \frac{r_0\cos\phi}{\sin\theta} \end{aligned}$$

Perform change of variable from r to ϕ using $\frac{\partial}{\partial r} = \frac{\partial}{\partial\phi}\cdot\frac{\partial\phi}{\partial r}$,

$$\begin{aligned} \dot{\varepsilon}_r &= \frac{\partial}{\partial\phi}\left(\frac{\sin\theta}{r_0\cos\phi}\cdot r\dot{\varepsilon}_c\right) + \dot{\varepsilon}_c\tan^2\phi + \cot\theta\tan^2\phi \\ &= \frac{\partial}{\partial\phi}\left(\frac{\cancel{\sin\theta}}{\cancel{r_0}\cos\phi}\cdot\frac{\cancel{r_0}\sin\phi}{\cancel{\sin\theta}}\cdot\dot{\varepsilon}_c\right) + \dot{\varepsilon}_c\tan^2\phi + \cot\theta\tan^2\phi \\ &= \frac{\partial}{\partial\phi}(\dot{\varepsilon}_c\tan\phi) + \cancel{\dot{\varepsilon}_c\tan^2\phi}^{\,0} + \cot\theta\tan^2\phi \\ &\quad \text{(small angle approximation)} \\ \therefore \dot{\varepsilon}_r &\approx \frac{\partial}{\partial\phi}(\dot{\varepsilon}_c\tan\phi) + \cot\theta\tan^2\phi \end{aligned} \tag{17}$$

Substitute Eq. (17) into Eq. (14),

$$\begin{aligned} \dot{\varepsilon} &= \dot{\varepsilon}_c + \dot{\varepsilon}_r \\ \dot{\varepsilon} &= \dot{\varepsilon}_c + \frac{\partial}{\partial\phi}(\dot{\varepsilon}_c\tan\phi) + \cot\theta\tan^2\phi \\ \frac{\partial}{\partial\phi}(\dot{\varepsilon}_c\tan\phi) + \dot{\varepsilon}_c &= \dot{\varepsilon} - \cot\theta\tan^2\phi \\ \sin\phi\left[\frac{\partial}{\partial\phi}(\dot{\varepsilon}_c\tan\phi) + \dot{\varepsilon}_c\right] &= \left(\dot{\varepsilon} - \cot\theta\tan^2\phi\right)\sin\phi \\ \sin\phi\left[\frac{\partial\dot{\varepsilon}_c}{\partial\phi}\tan\phi + \dot{\varepsilon}_c\sec^2\phi + \dot{\varepsilon}_c\right] &= \left(\dot{\varepsilon} - \cot\theta\tan^2\phi\right)\sin\phi \\ \frac{\partial\dot{\varepsilon}_c}{\partial\phi}\sin\phi\tan\phi + \dot{\varepsilon}_c\tan\phi\sec\phi + \dot{\varepsilon}_c\sin\phi &= \left(\dot{\varepsilon} - \cot\theta\tan^2\phi\right)\sin\phi \end{aligned}$$

$$\begin{aligned}
\text{Since} \quad \frac{\partial}{\partial\phi}(\dot{\varepsilon}_c \sin\phi\tan\phi) &= \frac{\partial\dot{\varepsilon}_c}{\partial\phi}\sin\phi\tan\phi + \dot{\varepsilon}_c\frac{\partial}{\partial\phi}(\sin\phi\tan\phi) \\
&= \frac{\partial\dot{\varepsilon}_c}{\partial\phi}\sin\phi\tan\phi + \dot{\varepsilon}_c[\sin\phi\sec^2\phi + \cos\phi\tan\phi] \\
&= \frac{\partial\dot{\varepsilon}_c}{\partial\phi}\sin\phi\tan\phi + \dot{\varepsilon}_c\tan\phi\sec\phi + \dot{\varepsilon}_c\sin\phi \\
\therefore \frac{\partial}{\partial\phi}(\dot{\varepsilon}_c \sin\phi\tan\phi) &= \left(\dot{\varepsilon} - \cot\theta\tan^2\phi\right)\sin\phi \qquad (18)
\end{aligned}$$

Considering a special case (at the top of the dome)

$$\dot{\varepsilon}_r = \frac{\partial}{\partial\phi}\left(\dot{\varepsilon}_c\tan\phi\right) + \cot\theta\tan^2\phi$$

For $\dot{\varepsilon}_r = \dot{\varepsilon}_c$,

$$\begin{aligned}
\dot{\varepsilon}_c &= \frac{\partial}{\partial\phi}\left(\dot{\varepsilon}_c\tan\phi\right) + \cot\theta\tan^2\phi \\
\frac{\partial}{\partial\phi}\left(\dot{\varepsilon}_c\tan\phi\right) - \dot{\varepsilon}_c &= -\cot\theta\tan^2\phi \\
\frac{1}{\sin\phi}\left[\frac{\partial}{\partial\phi}\left(\dot{\varepsilon}_c\tan\phi\right) - \dot{\varepsilon}_c\right] &= -\cot\theta\sec\phi\tan\phi \\
\frac{1}{\sin\phi}\left(\frac{\partial\dot{\varepsilon}_c}{\partial\phi}\tan\phi + \dot{\varepsilon}_c\sec^2\phi - \dot{\varepsilon}_c\right) &= -\cot\theta\sec\phi\tan\phi \\
\frac{\partial\dot{\varepsilon}_c}{\partial\phi}\sec\phi + \dot{\varepsilon}_c\sec\phi\tan\phi &= -\cot\theta\sec\phi\tan\phi
\end{aligned}$$

Since $\frac{\partial}{\partial\phi}\left(\dot{\varepsilon}_c\sec\phi\right) = \frac{\partial\dot{\varepsilon}_c}{\partial\phi}\sec\phi + \dot{\varepsilon}_c\sec\phi\tan\phi$,

$$\therefore \frac{\partial}{\partial\phi}\left(\dot{\varepsilon}_c\sec\phi\right) = -\cot\theta\sec\phi\tan\phi \qquad (19)$$

Using boundary condition $\dot{\varepsilon}_c = 0$ at $\phi = \theta$, assuming $\dot{\varepsilon}_c = \frac{\cos\phi - \cos\theta}{\sin\theta} = \dot{\varepsilon}_r$,

$$\begin{aligned}
\text{Since} \quad \frac{\partial}{\partial\phi}\left(\frac{\cos\phi - \cos\theta}{\sin\theta}\cdot\sec\phi\right) &= \frac{\partial}{\partial\phi}(\text{cosec}\theta - \cot\theta\sec\phi) \\
&= -\cot\theta\sec\phi\tan\phi \\
\therefore \dot{\varepsilon}_c &= \frac{\cos\phi - \cos\theta}{\sin\theta} \quad \text{is a solution.} \qquad (20)
\end{aligned}$$

Using the incompressibility condition,

$$\begin{aligned}\dot{\varepsilon} &= \dot{\varepsilon}_c + \dot{\varepsilon}_r \\ &= \frac{2(\cos\phi - \cos\theta)}{\sin\theta}\end{aligned}$$

Consider
$$\begin{aligned}&(1+\cos\phi)\tan\frac{\theta}{2} - (1-\cos\phi)\cot\frac{\theta}{2} \\ =\ & \frac{(1+\cos\phi)\sin\theta}{1+\cos\theta} - \frac{(1-\cos\phi)(1+\cos\theta)}{\sin\theta} \\ =\ & \frac{(1+\cos\phi)\sin^2\theta - (1-\cos\phi)(1+\cos\theta)^2}{\sin\theta(1+\cos\theta)} \\ =\ & \frac{\sin^2\theta + \cos\phi\sin^2\theta - (1-\cos\phi)(1+2\cos\theta+\cos^2\theta)}{\sin\theta(1+\cos\theta)} \\ =\ & \frac{\sin^2\theta + \cos\phi\sin^2\theta - 1 - 2\cos\theta - \cos^2\theta + \cos\phi + 2\cos\phi\cos\theta + \cos\phi\cos^2\theta}{\sin\theta(1+\cos\theta)} \\ =\ & \frac{2\cos\phi + 2\cos\phi\cos\theta - 1 - 2\cos\theta + \sin^2\theta - \cos^2\theta}{\sin\theta(1+\cos\theta)} \\ =\ & \frac{2\cos\phi(1+\cos\theta) - 2(1+\cos\theta) + (1+1-2\cos^2\theta)}{\sin\theta(1+\cos\theta)} \\ =\ & \frac{2\cos\phi\cancel{(1+\cos\theta)} - 2\cancel{(1+\cos\theta)} + 2(1-\cos\theta)\cancel{(1+\cos\theta)}}{\sin\theta\cancel{(1+\cos\theta)}} \\ =\ & \frac{2\cos\phi - \cancel{2} + \cancel{2} - 2\cos\theta}{\sin\theta} \\ =\ & \frac{2(\cos\phi - \cos\theta)}{\sin\theta} \\ =\ & \dot{\varepsilon}\end{aligned}$$

$$\therefore \dot{\varepsilon} = (1+\cos\phi)\tan\frac{\theta}{2} - (1-\cos\phi)\cot\frac{\theta}{2} \tag{21}$$

This is a special solution, studied by Hill (1950).

A proposed general solution:

$$\therefore \dot{\varepsilon} = (1+\lambda\cos\phi)\tan\frac{\theta}{2} - \lambda(1-\cos\phi)\cot\frac{\theta}{2} \tag{22}$$

where λ is an unknown parameter depending on the strain-hardening property of material and possibly also on the stage of the bulge.

When $\lambda = 1$,

Eq. (22) reduces to Eq. (21).

When $\lambda = 0$,

Eq. (22) corresponds to the assumption of Ross and Prager (1954), which assumed that the bulge is of uniform thickness at each stage, implying that $\dot{\varepsilon}$ is independent of ϕ.

$\therefore$ For all realistic cases, $0 < \lambda < 1$.

From Eq. (9),

$$\begin{aligned} w_0 &= r_0 \tan\frac{\theta}{2} \\ &\Rightarrow \sin\frac{\theta}{2} = \frac{w_0}{\sqrt{r_0^2 + w_0^2}}, \quad \cos\frac{\theta}{2} = \frac{r_0}{\sqrt{r_0^2 + w_0^2}} \\ \frac{dw_0}{d\theta} &= \frac{r_0}{2}\sec^2\frac{\theta}{2} \end{aligned}$$

Perform change of variable from θ to w_0,

$$\begin{aligned} \frac{d\varepsilon}{d\theta} &= \dot{\varepsilon} \\ \frac{d\varepsilon}{dw_0}\cdot\frac{dw_0}{d\theta} &= (1+\lambda\cos\phi)\tan\frac{\theta}{2} - \lambda(1-\cos\phi)\cot\frac{\theta}{2} \\ \frac{d\varepsilon}{dw_0} &= \frac{2}{r_0}\cos^2\frac{\theta}{2}\left[(1+\lambda\cos\phi)\tan\frac{\theta}{2} - \lambda(1-\cos\phi)\cot\frac{\theta}{2}\right] \\ &= \frac{2}{r_0}\left[(1+\lambda\cos\phi)\sin\frac{\theta}{2}\cos\frac{\theta}{2} - \lambda(1-\cos\phi)\frac{\cos^3\frac{\theta}{2}}{\sin\frac{\theta}{2}}\right] \\ &= \frac{2}{r_0}\left[(1+\lambda\cos\phi)\frac{r_0 w_0}{r_0^2+w_0^2} - \lambda(1-\cos\phi)\frac{r_0^3}{w_0(r_0^2+w_0^2)}\right] \end{aligned}$$

Substitute Eq. (11) into this expression,

$$\frac{d\varepsilon}{dw_0} = \frac{2}{\cancel{r_0}}\left\{\left[1+\lambda\left(1-\frac{2r^2w_0^2}{(r_0^2+w_0^2)^2}\right)\right]\frac{\cancel{r_0}w_0}{r_0^2+w_0^2} - \lambda\left[\frac{2r_0\cancel{w_0^2}}{(r_0^2+w_0)^2}\right]\frac{r_0^{\cancel{2}}}{\cancel{w_0}(r_0^2+w_0^2)}\right\}$$

$$
\begin{aligned}
&= \frac{2w_0}{r_0^2+w_0^2}\left[1+\lambda-\lambda\frac{2r^2w_0^2}{(r_0^2+w_0^2)^2}-\lambda\frac{2r^2r_0^2}{(r_0^2+w_0^2)^2}\right] \\
&= \frac{2w_0}{r_0^2+w_0^2}\left[(1+\lambda)-\frac{2r^2\lambda}{r_0^2+w_0^2}\right] \qquad (23)
\end{aligned}
$$

At the pole, $\phi = 0 \Rightarrow \cos\phi = 1$.
From Eq. (11),

$$\frac{2r^2w_0^2}{(r_0^2+w_0^2)^2} = 0$$

From Eq. (23),

$$
\begin{aligned}
\frac{d\varepsilon}{dw_0} &= \frac{2w_0}{r_0^2+w_0^2}\left[(1+\lambda)-\frac{2r^2\lambda}{r_0^2+w_0^2}\right] \\
&= (1+\lambda)\frac{2w_0}{r_0^2+w_0^2} - \cancelto{0 \text{ at the pole}}{\frac{2r^2w_0^2}{(r_0^2+w_0^2)^2}}\cdot\frac{2\lambda}{w_0} \\
\frac{d\varepsilon_0}{dw_0} &= (1+\lambda)\frac{2w_0}{r_0^2+w_0^2} \qquad (24) \\
&\quad \text{where } \varepsilon_0 \text{ is the through-thickness strain.}
\end{aligned}
$$

Assume λ depends only on the strain-hardening characteristic of material, let $\lambda = 1-n$ for $0 < \lambda < 1$, where n is the strain-hardening index in $\sigma = K\varepsilon^n$.

$$\therefore \frac{d\varepsilon_0}{dw_0} = (2-n)\frac{2w_0}{r_0^2+w_0^2}$$

Integrate with respect to w_0,

$$\varepsilon_0 = (2-n)\ln\left(1+\frac{w_0^2}{r_0^2}\right) \qquad (25)$$

Since $\varepsilon_0 = -\ln\left(\frac{h}{h_0}\right)$, where the negative sign indicates a compression,

$$
\begin{aligned}
\frac{h_0}{h} &= \left(1+\frac{w_0^2}{r_0^2}\right)^{2-n} \\
\frac{h_0}{h} &= \left(\frac{r_0^2+w_0^2}{r_0^2}\right)^{2-n}
\end{aligned}
$$

$$\begin{aligned} \frac{h}{h_0} &= \left(\frac{r_0^2}{r_0^2 + w_0^2}\right)^{2-n} \\ \therefore h &= h_0 \left[\frac{1}{1 + \left(\frac{w_0}{r_0}\right)^2}\right]^{2-n} \end{aligned} \tag{26}$$